

Assessment of MERRA-2 Land Surface Energy Flux Estimates

Clara S. Draper *

USRA/GESTAR and NASA Global Modeling and Assimilation Office, Greenbelt, MD, USA.

Now at CIRES NOAA/ESRL, Physical Sciences Division, Boulder, CO.

Rolf H. Reichle

NASA Global Modeling and Assimilation Office, Greenbelt, MD, USA.

Randal D. Koster

NASA Global Modeling and Assimilation Office, Greenbelt, MD, USA.

*Corresponding author address: Clara Draper, NOAA ESRL, Physical Sciences Division, 325

Broadway, Boulder, CO, USA.

E-mail: clara.draper@noaa.gov

ABSTRACT

12 In the Modern-Era Retrospective analysis for Research and Applications,
13 version 2 (MERRA-2) system the land is forced by replacing the model-
14 generated precipitation with observed precipitation before it reaches the sur-
15 face. This approach is motivated by the expectation that the resultant improve-
16 ments in soil moisture will lead to improved land surface latent heating (LH).
17 Here we assess aspects of the MERRA-2 land surface energy budget and 2 m
18 air temperatures (T^{2m}). For global land annual averages, MERRA-2 appears
19 to overestimate the LH (by 5 Wm^{-2}), the sensible heating (by 6 Wm^{-2}),
20 and the downwelling shortwave radiation (by 14 Wm^{-2}), while underestimat-
21 ing the downwelling and upwelling (absolute) longwave radiation (by 10-15
22 Wm^{-2} each). These results differ only slightly from those for NASA's previ-
23 ous reanalysis, MERRA. Comparison to various gridded reference data sets
24 over Boreal summer (June-July-August) suggests that MERRA-2 has particu-
25 larly large positive biases ($>20 \text{ Wm}^{-2}$) where LH is energy-limited, and that
26 these biases are associated with evaporative fraction biases rather than radi-
27 ation biases. For time series of monthly means during Boreal summer, the
28 globally averaged anomaly correlations (R_{anom}) with reference data were im-
29 proved from MERRA to MERRA-2, for LH (from 0.39 to 0.48 vs. GLEAM
30 data) and the daily maximum T^{2m} (from 0.69 to 0.75 vs. CRU data). In re-
31 gions where T^{2m} is particularly sensitive to the precipitation corrections (in-
32 cluding the central US, the Sahel, and parts of south Asia), the changes in
33 the $T^{2m} R_{anom}$ are relatively large, suggesting that the observed precipitation
34 influenced the T^{2m} performance.

35 **1. Introduction**

36 The NASA Global Modeling and Assimilation Office recently released the Modern-Era Ret-
37 rospective analysis for Research and Applications, version 2 (MERRA-2; Gelaro and Coauthors
38 (2017)). This new global reanalysis product replaces and extends the original MERRA atmo-
39 spheric reanalysis (Rienecker et al. 2011), as well as the MERRA-Land reanalysis (Reichle et al.
40 2011). In addition to several other major advances, MERRA-2 uses observed precipitation in place
41 of model-generated precipitation at the land surface during the atmospheric model integration. The
42 use of observed precipitation in MERRA-2 was refined from the approach used for MERRA-Land
43 (Reichle et al. 2017b), which was an offline (land only) replay of MERRA forced by atmospheric
44 fields from MERRA but with the precipitation forcing corrected using gauge-based observations.

45 The motivation for using observed precipitation in reanalyses is that precipitation is the main
46 driver of soil moisture, which in turn controls the partitioning of incident surface radiation between
47 latent heat (LH) and sensible heat (SH) fluxes back to the atmosphere. Reichle et al. (2017a)
48 show that both MERRA-2 and MERRA-Land have improved upon the land surface hydrology of
49 MERRA, showing better agreement with independent observational time series of soil moisture,
50 terrestrial water storage, stream flow, and snow amount. Here, we extend this work, by evaluating
51 the MERRA-2 surface energy budget and 2 m temperatures (T^{2m}) over land. In particular, we
52 focus on whether the improved hydrology in both the (offline) MERRA-Land and the (coupled
53 land/atmosphere) MERRA-2 data sets translates into the expected improvements to the monthly
54 mean LH and SH. We also expand previous work by evaluating the reanalyses land surface output
55 globally, rather than focusing on locations with high quality ground-based observations.

56 We start by comparing the long-term annual global energy budget over land from MERRA-2,
57 MERRA-Land, and MERRA to state of the art estimates from the literature. These literature

58 estimates, from Trenberth et al. (2009), Wild et al. (2015), and the NASA Energy and Water Cycle
59 Studies program (NEWS, NSIT (2007); L'Ecuyer et al. (2015)) were each produced by carefully
60 combining multiple input data sets with global energy balance constraints. Taken together they
61 represent our best understanding of the long-term annual mean energy budget over land.

62 Next, we consider global maps of the performance of the land surface turbulent heat fluxes from
63 each reanalyses, as a step towards linking differences in performance to the dominant local physi-
64 cal processes and to the potential improvements obtained from the use of the observed precipitation
65 in MERRA-2. We focus on the Boreal summer (June-July-August; JJA), since land/atmosphere
66 coupling is strongest and surface turbulent heat fluxes are most active in the summer.

67 Unfortunately, there are no standard global gridded reference data sets against which the reanal-
68 ysis LH and SH can be evaluated. Several recent efforts have compared global LH estimates from
69 different combinations of reanalyses, offline land surface models, and diagnostic methods. Most
70 estimates generally agree on the regional patterns and local seasonal cycle of LH, although there
71 is considerable disagreement in the absolute values and temporal behavior across different flux
72 estimates (Jiménez et al. 2011; Mueller et al. 2011; Miralles et al. 2011). Additionally, uncer-
73 tainty in the basic model structure is the largest source of disagreement (Schlosser and Gao 2010;
74 Mueller et al. 2013). While ground-based observations are available from tower-mounted eddy
75 covariance sensors (e.g., Baldocchi and Coauthors (2001)), the number of towers (in the 100's)
76 is well below the sampling needed for global estimation (and their locations are not designed to
77 sample globally-representative land cover types). Additionally, the measurements themselves have
78 considerable uncertainty and limited spatial representativeness (up to 1 km).

79 In the absence of a standard reference, we compare the JJA reanalysis turbulent heat flux esti-
80 mates to two different gridded reference data sets: Global Land surface Evaporation: the Ams-
81 terdam Methodology (GLEAM) (Miralles et al. 2011; Martens et al. 2017) for LH, and Fluxnet-

82 Model Tree Ensembles (MTE) (Jung et al. 2010) for LH and SH. These data sets were selected for
83 several reasons: i) they are amongst the state of the art, ii) they are available globally for multi-
84 decadal time periods, iii) they are independent of each other, and iv) they rely on very different
85 estimation methodologies (water balance modeling for GLEAM, and upscaling of tower measure-
86 ments for MTE). Since neither GLEAM nor MTE represents direct observations of the turbulent
87 heat fluxes, we also compare each reanalysis to tower-based eddy covariance observations from
88 the Fluxnet-2015 data set (Fluxnet 2015). To determine the potential contribution of radiation bi-
89 ases to regional LH and SH biases, we also compare the reanalyses surface radiation fields for JJA
90 against gridded observations from the Clouds and the Earth’s Radiant Energy System (CERES)
91 and Energy Balanced and Filled (EBAF) data set (Kato et al. 2013).

92 Finally, to test whether the changes in the surface energy budget from MERRA to MERRA-
93 2 have affected the atmospheric boundary layer, we also evaluate the JJA monthly mean daily
94 minimum and maximum T^{2m} against observations from the Climatic Research Unit (CRU) at the
95 University of East Anglia (Harris et al. 2014). Improvements in MERRA-2 due to the use of
96 observed precipitation cannot be isolated from the many other advances distinguishing MERRA-
97 2 from MERRA. Consequently, we establish whether the improvements in the surface turbulent
98 fluxes and T^{2m} are at least consistent with the expected improvements from the use of observed
99 precipitation, by cross-referencing the evaluation results against the regional sensitivity to precip-
100 itation and/or soil moisture.

101 This paper is organized as follows. Section 2 summarizes the reanalysis and reference data sets
102 used, and Section 3 presents the results, including evaluation of the i) reanalyses annual global
103 land energy budget averages, ii) the spatially distributed mean JJA energy budget and T^{2m} , and ii)
104 the temporal behavior of the JJA turbulent heat fluxes and T^{2m} . We also identify regions of sensi-

105 tivity to the observed precipitation forcing in MERRA-2, for cross-reference against the evaluation
106 results. Our findings are summarized in Section 4.

107 **2. Methodology and data**

108 *a. The reanalyses*

109 The coverage and resolution of each reanalysis is summarized in Table 1, with further details
110 below. MERRA (Rienecker et al. 2011) and MERRA-2 (Gelaro and Coauthors 2017) are atmo-
111 spheric reanalyses produced with the NASA Goddard Earth Observing System Version 5 (GEOS-
112 5) modeling and data assimilation system, and were designed to provide historical analyses of the
113 hydrological cycle across a broad range of climate time scales. To address shortcomings in the
114 MERRA land surface hydrology, MERRA-Land (Reichle et al. 2011) was released as an offline
115 (land only) replay of MERRA, with the model-generated precipitation corrected using rain-gauge
116 observations and with minor, but important, model parameter changes. MERRA-2 features sev-
117 eral major advances from MERRA, including an updated atmospheric general circulation model,
118 an updated atmospheric assimilation system, an interactive aerosol scheme, and the use of ob-
119 served precipitation at the land surface (and to compute wet aerosol deposition). In addition to
120 the land model updates from MERRA-Land, MERRA-2 includes several more updates relevant to
121 the land, as outlined in Reichle et al. (2017a). Most notably, the surface turbulence scheme was
122 revised, generally resulting in enhanced SH over land (Molod et al. 2015).

123 The method used to apply the observed precipitation at the land surface in MERRA-2 was refined
124 from that used in MERRA-Land (Reichle and Liu 2014; Reichle et al. 2017b). In MERRA-Land
125 the precipitation was corrected with daily Climate Prediction Center (CPC) Unified (CPCU; Chen
126 et al. (2008)) precipitation observations everywhere. For MERRA-2 the input precipitation differs

127 in two ways: i) in the high latitudes the MERRA-2 model-generated precipitation is retained, and
128 ii) over Africa the MERRA-2 precipitation is corrected with pentad-scale blended satellite and
129 gauge-based observations from the CPC Merged Analysis of Precipitation (CMAP; Xie and Arkin
130 (1997)) and the Global Precipitation Climatology Project (GPCP; Huffman et al. (2009)) version
131 2.1.

132 The land surface turbulent fluxes from the NASA reanalyses (MERRA-2, MERRA-Land, and
133 MERRA) have not been explicitly evaluated globally. However, Jiménez et al. (2011) and Mueller
134 et al. (2011) both included MERRA LH when merging multiple LH global land data sets into a
135 single enhanced estimate (see Section 2.b), and in both studies MERRA was amongst the high-
136 est of the input LH estimates used. Additionally, Jiménez et al. (2011) noted a sharp gradient
137 in the MERRA LH around 10°S in the tropics that was not present in other LH estimates. This
138 bias gradient was traced to MERRA's excessive rainfall canopy interception and precipitation er-
139 rors (Reichle et al. 2011). Consequently, the interception reservoir parameters were revised for
140 MERRA-Land (and MERRA-2) to eliminate this feature (the interception reservoir update was
141 the most significant modeling change from MERRA to MERRA-Land).

142 An additional reanalysis, ERA-Interim, from the European Centre for Medium Range Weather
143 Forecasting (Dee et al. 2011), is included in the evaluation of the temporal behavior of the turbulent
144 fluxes. In contrast to the NASA reanalyses, ERA-Interim includes a land surface updating scheme
145 (de Rosnay et al. 2014). Specifically, the soil moisture, soil temperature, and snow temperatures
146 are updated to minimize errors in the forecast screen-level relative humidity and temperature,
147 while the snow depths are updated using satellite- and ground-based snow cover and snow depth
148 observations.

149 *b. Annual global land energy budget estimates*

150 We compare the reanalyses annual global land energy budgets to three state of the art estimates,
151 from Trenberth et al. (2009), Wild et al. (2015), and the NEWS program estimates of L'Ecuyer
152 et al. (2015). Each of these is based on a weighted merger of multiple modeled and observed data
153 sets, and each applies to the energy budget at the start of the 21st Century. For Trenberth et al.
154 (2009) we have used their estimates for the 'CERES period' of 2000-2004; Wild et al. (2015)
155 nominally refers to the same period; while L'Ecuyer et al. (2015) nominally refers to 2000-2009.
156 Note that the MERRA LH and SH over land were used as one of the inputs in NEWS.

157 These three global energy budget studies all provide continental and oceanic energy estimates,
158 where 'continental' is defined as non-ocean, and so includes land, land-ice, and lakes, but excludes
159 inland seas. By contrast, the land estimates from MERRA-2, MERRA-Land, and MERRA apply
160 to the area modeled by the land surface model, excluding land-ice, lakes, and inland seas. The
161 discrepancy due to the inclusion or exclusion of land-ice is significant: land-ice accounts for 10%
162 of the continental area, with Antarctica making up 95% of this. NEWS provides energy bud-
163 gets for each continent separately (L'Ecuyer et al. 2015), and we use their (balance-constrained)
164 energy budget estimates to approximate the land-only energy budget terms by subtracting the area-
165 weighted Antarctica estimates from the global continental estimates. We then use our land-only
166 NEWS estimates to approximate the continental to land ratio for each NEWS energy budget term.
167 By assuming that the same ratios apply to Trenberth et al. (2009) and Wild et al. (2015) we then
168 approximate land-only estimates for the latter two studies. L'Ecuyer et al. (2015) and Wild et al.
169 (2015) both provide uncertainty ranges for their globally averaged continental estimates, which
170 we have applied unchanged to our approximated land-only estimates.

171 For LH, we have also used three additional global land annual average estimates from the hy-
172 drology community, from Jiménez et al. (2011), Mueller et al. (2011), and Mueller et al. (2013).
173 These estimates are also based on merging modeled and observed estimates. Jiménez et al. (2011)
174 applies to global land (using a similar land definition to the NASA reanalyses) for 1994, while
175 Mueller et al. (2011) applies to the global land area, excluding the Sahara, from 1989-1995, and
176 Mueller et al. (2013) applies to the global land plus Greenland for 1989-2005. As previously noted,
177 MERRA LH was one of the inputs used in the multi-product mergers of Jiménez et al. (2011) and
178 Mueller et al. (2011).

179 *c. Gridded reference data sets*

180 The coverage and resolution of each gridded reference data set, together with a brief summary
181 of important interdependencies with other data sets or reanalyses used in the study and uncertainty
182 estimates (where available) are summarized in Table 2, with further details provided below.

183 1) GLEAM

184 GLEAM (version 3.1a) provides daily estimates of terrestrial evapotranspiration, estimated from
185 satellite and reanalysis forcing using a Priestley and Taylor-based model (Miralles et al. 2011;
186 Martens et al. 2017). The precipitation is from the Multi-Source Weighted-Ensemble Precipitation,
187 which is a multi-model merger of established precipitation data sets, including the same CPCU
188 data set used in MERRA-Land and MERRA-2, as well as ERA-Interim precipitation (the latter is
189 used predominantly in the high latitudes, where observed precipitation data sets are more uncertain
190 (Beck et al. 2017)). The net surface radiation and T^{2m} are from ERA-Interim. Compared to
191 independent observations from 91 flux towers, GLEAM has an average unbiased root mean square

192 error (ubRMSE; or error standard deviation) of 20 Wm^{-2} and an average anomaly correlation of
193 0.42 (Martens et al. 2017).

194 2) MTE

195 MTE provides global estimates of carbon dioxide, energy, and water fluxes at the land surface,
196 calculated using a machine learning technique to upscale half-hourly energy balance-corrected
197 eddy covariance observations from 253 Fluxnet tower observations (Jung et al. 2011). The input
198 Fluxnet observations are from the La Thuile data release, an earlier generation of the Fluxnet-
199 2015 data set used here (to be introduced in Section 2.d). CPCU precipitation (again, used directly
200 in MERRA-Land and MERRA-2) and a T^{2m} data set based on CRU data (Jung et al. 2011) are
201 used as predictive (regression) variables in the MTE. However, this meteorological data has little
202 impact on the MTE monthly anomalies, which are instead driven by the vegetation variability
203 as observed by the fraction of absorbed Photosynthetically Active Radiation (fPAR; Jung et al.
204 (2010)). When 20% of the Fluxnet training data was withheld from the algorithm, the average
205 Root Mean Square Error (RMSE) with the withheld data was 15 Wm^{-2} , for both LH and SH, and
206 the average anomaly correlation was 0.57 for LH and 0.60 for SH (Jung et al. 2011). In general,
207 the MTE method is better suited to estimating spatial variability and the seasonal cycle than it is
208 to capturing interannual anomaly patterns (Jung et al. 2009).

209 3) CRU TEMPERATURE DATA

210 CRU TSv4.00 provides gridded monthly means of the daily mean, minimum, and maximum
211 temperature over land (Harris et al. 2014; University of East Anglia Climate Research Unit et
212 al. 2014). The temperatures are calculated from quality controlled climate station data, which are
213 interpolated onto the grid according to an assumed correlation decay distance (set to 1200 km for

214 temperature variables). In instances where no station data are available within the assumed decay
215 distance, the published data value defaults to the climatology. Here, such climatological values
216 have been screened out. Also, we require at least 10 data points to estimate each statistic for a
217 given grid cell. Even with this screening, the gridded output will be much less certain when/where
218 station coverage is less dense, which occurs over Africa, South America, central Australia, and the
219 high latitudes.

220 4) CERES-EBAF RADIATION DATA

221 CERES-EBAF version 4.00 surface radiances are produced with a radiative transfer model af-
222 ter adjusting modeled and observed input data for consistency with Top of Atmosphere (TOA)
223 CERES-EBAF radiation (Kato et al. 2013). The input data (surface, cloud, and atmospheric prop-
224 erties) are adjusted according to their observation-based estimated uncertainties. The input temper-
225 ature and humidity profiles and land surface skin temperature (T_{skin}) are from NASA's GEOS-5.4.1
226 modeling and assimilation system, the same system (although a different version) used in MERRA
227 and MERRA-2.

228 The CERES output shortwave irradiances are primarily determined by (observation-based) TOA
229 radiation and clouds, hence they are reasonably independent of the MERRA and MERRA-2 re-
230 analyses (Kato et al. 2013). On the other hand, the CERES output longwave irradiances, and
231 particularly the upwelling longwave (LW_u), are strongly dependent on the GEOS-5 T_{skin} input.
232 However, the CERES algorithm does adjust its input GEOS-5 T_{skin} with observation-based cloud
233 information, so comparison between the CERES-EBAF and GEOS-5 LW_u partly reflects these
234 observation-based adjustments, even though the two fields are not independent. Compared to in-
235 dependent ground-based observations from 24 sites over land, the RMSE of the CERES-EBAF
236 radiation is 12 Wm^{-2} for downwelling shortwave (SW_d), and 10 Wm^{-2} for downwelling long-

237 wave (LW_d) (CERES-EBAF 2017). For the regional estimates over land, CERES-EBAF (2017)
238 estimated the uncertainty to be 12 Wm^{-2} for SW_d , 4 Wm^{-2} for upwelling shortwave (SW_u), 10
239 Wm^{-2} for LW_d , and 18 Wm^{-2} for LW_u .

240 5) GRIDDED DATA SET PROCESSING

241 As noted in Tables 1 and 2 some of the reference data sets and reanalyses used here publish
242 output that applies only to the land fraction within each grid cell, while others publish a single
243 estimate that applies to all surface types (land, permanent land-ice, lakes, ocean) within each grid
244 cell. All of the gridded data sets and reanalyses were screened by removing all grid cells where
245 the MERRA-2 land fraction was less than 50% (after interpolation to the relevant resolution), and
246 then aggregated up to monthly means and 1° spatial resolution. All maps of global statistics are
247 based on the Boreal summer months of JJA only, and each comparison is made over the maximum
248 available co-incident time period, with the time periods noted in the relevant figure captions. The
249 anomaly correlations (R_{anom}) are evaluated based on anomalies from the mean seasonal cycle
250 (calculated by subtracting the time period mean separately for each calendar month). The gridded
251 reference data sets were also used to estimate the annual global land average values, for which the
252 (interpolated) MERRA-2 land area in each grid cell was used.

253 *d. Fluxnet-2015 tower observations*

254 The Fluxnet-2015 (Fluxnet 2015) sites were selected by downloading all Tier 1 observations at
255 non-irrigated sites within grid cells classified as land at 1° resolution (as derived above in Section
256 2.c.5), and for which at least a 10 year data record is available. Eddy covariance sensors underesti-
257 mate turbulent heat fluxes and do not generally close the energy balance (Wilson et al. 2002), hence
258 we used the Fluxnet-2015 energy balance closure-corrected LH and SH (see Fluxnet (2015) for

259 details of the correction method). While these corrections are rather uncertain, the corrected LH
260 and SH showed better agreement with all of the reanalyses in Table 1 in terms of the means across
261 all sites and the correlation of the means between the sites (while having negligible impact on the
262 mean time series anomaly correlations). The balance-corrected Fluxnet data were then screened
263 to retain only days with less than 10% gap-filled data, and only sites with data for at least 2550
264 days ($\sim 70\%$ of 10 years). The monthly means were then calculated for months with at least 15
265 days of observations after the above screening, and the corresponding reanalysis monthly means
266 were estimated using the same days. The resulting Fluxnet monthly time series were visually in-
267 spected, and obviously unrealistic features were removed. Four sites with unrealistic time series
268 were removed. Of the remaining 21 stations, just one was in the Southern Hemisphere. Since our
269 evaluation focuses on the Boreal summertime, this site was excluded. The remaining 20 sites that
270 have been used in this study are listed in supplemental Table 1.

271 **3. Results**

272 *a. Annual global land energy budgets*

273 The globally averaged annual land energy budget estimates for MERRA-2, MERRA-Land, and
274 MERRA are illustrated in Figure 1, with numerical values given in Table 3. For each term, the
275 estimates for MERRA-2 and MERRA are similar (within $2\text{-}3\text{ }Wm^{-2}$), while the partitioning of
276 R_{net} into LH and SH differs for MERRA-Land, which is shifted towards greater SH. Compared to
277 MERRA, MERRA-Land has $11\text{ }Wm^{-2}$ more SH, and $8\text{ }Wm^{-2}$ less LH, with the difference in R_{net}
278 due to decreased LW_u (recall that in the offline MERRA-Land SW_{net} and LW_d are taken directly
279 from MERRA).

280 Figure 1 also includes the energy budget estimates from the literature (see Section 2.b), as well
281 as the annual global land averages for each of the gridded reference data sets in Table 2. In Figure
282 1a, the MERRA-2 and MERRA global land LH are higher than all of the other estimates (although
283 MERRA-2 is within the Jiménez et al. (2011) and Wild et al. (2015) confidence intervals). The
284 three (land-adjusted) LH estimates from the global energy budget studies (Trenberth et al. (2009),
285 Wild et al. (2015), and NEWS) are very similar to each other, and to MTE, GLEAM, Mueller et al.
286 (2011), and MERRA-Land (all are within 1 Wm^{-2}). While the other two LH estimates from the
287 hydrology community (Jiménez et al. (2011) and Mueller et al. (2013)) are higher, they are not as
288 high as MERRA-2 and MERRA. Compared to the average of the three global land energy budget
289 estimates, the MERRA-2 LH is biased high by 6 Wm^{-2} (15%), while MERRA is biased high by
290 9 Wm^{-2} (21%), and MERRA-Land is much closer, being biased high by just 1 Wm^{-2} (2%).

291 For the global land SH in Figure 1b, MERRA-2 and MERRA are both higher than Trenberth
292 et al. (2009) and Wild et al. (2015), although lower than NEWS (but within the NEWS confidence
293 interval) and very close (within 1 Wm^{-2}) to MTE. Compared to the average of the three global
294 land energy budget estimates, MERRA-2 is biased high by 5 Wm^{-2} (15%) and MERRA by 4
295 Wm^{-2} (12%), while MERRA-Land is much higher, with a bias of 15 Wm^{-2} (42%).

296 The positive biases in both LH and SH from the reanalyses indicate a positive bias in the incident
297 energy at the land surface. Indeed, Figure 1g shows that the reanalyses R_{net} exceed the three
298 global energy budget estimates, although MERRA-2 (the lowest of the reanalyses) is only slightly
299 higher (2 Wm^{-2}) than the CERES-EBAF value. Compared to the average of the three global
300 energy budget estimates, the R_{net} biases are 12 Wm^{-2} (15%) for MERRA-2, 13 Wm^{-2} (17%) for
301 MERRA, and 16 Wm^{-2} (21%) for MERRA-Land. Figures 1c-f show that the positive R_{net} bias in
302 MERRA-2 and MERRA is made up of a large positive bias in SW_d combined with insufficient LW_u ,
303 both partly offset by underestimated LW_d . For SW_d (Figure 1c) MERRA-2 and MERRA are higher

304 than all three global land energy budget estimates and CERES-EBAF, with a bias compared to the
305 the three-product average of 14 Wm^{-2} (7%) for MERRA-2 and 16 Wm^{-2} (8%) for MERRA.
306 For SW_u (Figure 1d), MERRA-2 and MERRA are both above NEWS, Trenberth et al. (2009),
307 and CERES-EBAF, but below Wild et al. (2015) (although within the confidence interval). Both
308 are biased high by 3 Wm^{-2} (8%), compared to the three-product average. For LW_d (Figure 1e),
309 MERRA-2 and MERRA are lower than the of the other estimates, with biases of -11 Wm^{-2} (-
310 3%) for MERRA-2 and -10 Wm^{-2} (-3%) for MERRA against the three-product average. For
311 LW_u (Figure 1f) MERRA-2, MERRA-Land, and MERRA are again lower than the other plotted
312 estimates, with biases of -11 Wm^{-2} (-3%) for MERRA-2, -13 Wm^{-2} (-3%) for MERRA-Land,
313 and -10 Wm^{-2} (-3%) for MERRA.

314 The literature estimates in Figure 1 are presented as long term means, and each represents dif-
315 ferent temporal and spatial coverage. Likewise, the annual global land averages for the gridded
316 reference data sets in Figure 1 are based on the full available (spatial and temporal) coverage for
317 each. However, the gridded reference data sets and reanalyses can be cross-screened to ensure that
318 they are compared with consistent coverage. With this cross-screening, the MERRA-2 LH bias
319 estimate is 7 Wm^{-2} vs. GLEAM, or 9 Wm^{-2} vs. MTE, while the SH bias is 1 Wm^{-2} vs. MTE,
320 and the radiation biases vs. CERES-EBAF are 10 Wm^{-2} for SW_u , 2 Wm^{-2} for SW_d , -18 Wm^{-2} for
321 LW_d , -11 Wm^{-2} for LW_u , and $<0.5 \text{ Wm}^{-2}$ for R_{net} . In general, the above-quoted biases (calculated
322 after cross-screening) are all close (within 1 Wm^{-2}) to the values estimated from the data plotted
323 in Figure 1 (which does not include cross-screening), with the exception of the LH bias vs. MTE,
324 which is 6 Wm^{-2} without cross-screening (compared to 9 Wm^{-2}). This discrepancy is due to the
325 MTE global mean being lower than it otherwise would be, due to the lack of coverage over the
326 Sahara (which has near-zero annual mean LH).

327 *b. Land-atmosphere coupling and the MERRA-2 precipitation corrections*

328 Here, we identify regions where, in MERRA-2, i) LH is sensitive to precipitation (or soil mois-
329 ture), and ii) the daily maximum T^{2m} (T_{max}^{2m}) is sensitive to the applied precipitation corrections.
330 These regions can then be used to determine where the change in performance from MERRA to
331 MERRA-2 is most likely associated with the precipitation corrections. Note that for part ii) above,
332 the diurnal temperature range could be expected to have a stronger signal of the daytime turbulent
333 heat fluxes (Betts et al. 2017), however a preliminary comparison (not shown) revealed similar re-
334 sults for DTR and T_{max}^{2m} , and we have presented the results for T_{max}^{2m} since this variables is included
335 in the published MERRA-2 data sets.

336 1) SOIL MOISTURE AND LATENT HEATING

337 To first order, LH (or evapotranspiration) from soil and vegetation surfaces can be conceptu-
338 alized as either a moisture- or energy-limited process. In drier conditions (i.e., for soil moisture
339 below some critical point), LH is moisture-limited in that it is restricted by the amount of soil
340 moisture available for evapotranspiration. Temporal variations in LH will then be correlated with
341 the plant available soil moisture (principally, the soil moisture in the root-zone). In contrast, in
342 more humid conditions LH is energy limited; there is sufficient soil moisture available for evap-
343 otranspiration, so LH proceeds at the maximum rate determined by atmospheric water demand,
344 and temporal variations in LH are accordingly correlated with temporal variations in atmospheric
345 demand (net radiation, atmospheric humidity deficit, and wind), rather than soil moisture.

346 Figure 2 shows the squared correlation between the JJA monthly anomaly MERRA-2 LH and
347 rootzone soil moisture ($R_{anom}^2(LH, SM)$). Lower $R_{anom}^2(LH, SM)$ indicates a tendency towards
348 energy-limited LH, which for the Boreal summer occurs in the high latitudes, central and eastern
349 Europe, the eastern US, south China, and much of the tropics (the Amazon, equatorial Africa, and

southeast Asia). On the other hand, higher $R_{anom}^2(LH, SM)$ indicates a tendency towards moisture-limited LH, and occurs across the remainder of the low and mid-latitudes. While we have plotted JJA to focus on the Boreal summer, there are still regions of moisture-limited LH in the southern hemisphere during Austral winter, specifically in arid regions (southern Africa, much of Australia, and the desert and steppe regions of South America).

2) PRECIPITATION FEEDBACK ON AIR TEMPERATURE

Figure 3 shows maps of the squared anomaly correlation (R_{anom}^2) between anomaly timeseries of JJA MERRA-2 monthly T_{max}^{2m} and anomaly timeseries of 2-month (current + previous month) averaged MERRA-2 precipitation. For example, the June T_{max}^{2m} is compared to the (May+June) precipitation, while the July T_{max}^{2m} is compared to the (June+July) precipitation, and so on. The precipitation is lagged like this to allow the precipitation signal to accumulate in the soil, and influence the subsequent T_{max}^{2m} . In Figure 3a the MERRA-2 model-generated precipitation (PRECTOT) is used, while in Figure 3b the MERRA-2 observation-corrected precipitation (PRECTOTCORR) is used. The R_{anom}^2 are plotted only for negative R values, since the dominant local relationship between precipitation and daytime temperature is negative (i.e., under moisture-limited conditions, reduced precipitation leads to reduced soil moisture, which limits LH and increases SH and T^{2m}). Figure 3b reflects the modeled relationship in MERRA-2 between precipitation falling on the surface and T_{max}^{2m} . Even with the difference in time periods, the patterns are similar to those found across the contiguous U.S. from observations by Koster et al. (2015).

Figure 3c then shows the difference between $R_{anom}^2(T_{max}^{2m}, PRECTOTCORR)$ and $R_{anom}^2(T_{max}^{2m}, PRECTOT)$. This difference (ΔR_{anom}^2) is the increase in the fraction of variance in T_{max}^{2m} explained by the (observed) precipitation seen by the land (PRECTOTCORR) over that explained by the model-generated precipitation (PRECTOT). It thus provides a measure of

373 the local impact of the observed precipitation on the MERRA-2 T_{max}^{2m} . This measure is sensitive
374 to both the magnitude of the precipitation corrections and the local response of the atmospheric
375 model to those corrections. Note that the lack of sensitivity in the high latitudes was inevitable for
376 this metric, since the model-generated precipitation is used there.

377 For the Boreal summer, the strongest impact of the observed precipitation, which can explain
378 more than 25% of the T_{max}^{2m} variance, is indicated in the central US, central America, the northern
379 tip of South America, across a broad swath along the Sahel, and parts of south Asia. Note that
380 these regions do not directly correspond to the regions of strongest moisture-limited LH in Figure
381 2, for at least two reasons. First, a strong sensitivity of evapotranspiration to soil moisture (Figure
382 2) does not imply that the soil moisture variations are locally strong enough to induce large evap-
383 otranspiration variations and thus large impacts on air temperature (Figure 3c). Second, as noted
384 previously, the plotted sensitivity also includes a signal of the size of the precipitation corrections,
385 and so will be enhanced where the differences between the model-generated and observation-
386 corrected precipitation are larger.

387 Figure 3c is consistent with previous studies identifying hot-spots of strong coupling between
388 the land and T^{2m} . In particular Koster et al. (2006) and Miralles et al. (2012) both identify similar
389 regions of strong coupling centered on the central US/central America and the Sahel, although
390 they do not agree as well over south Asia. Over South Asia Koster et al. (2006) does not locate a
391 hotspot, while Miralles et al. (2012) identifies India as having the strongest coupling, and Figure
392 3c suggests patchy regions of coverage spanning from southeast Asia through the north of India.

393 For reference, the corresponding maps for the Austral summer (December-January-February)
394 are shown in supplemental Figure 1 for $R_{anom}^2(LH, SM)$ and supplemental Figure 2 for the sensi-
395 tivity to the precipitation corrections. In supplemental Figure 1, the $R_{anom}^2(LH, SM)$ over Austral
396 summer again shows the expected pattern of moisture-limited LH in drier areas of the summer

397 hemisphere (almost everywhere, outside of the tropics). As with the Boreal summer, regions of
398 moisture-limitation LH extend into the winter Hemisphere. However, the effect of reduced radia-
399 tion close to the poles is now evident in the switch to energy-limited LH, even in arid regions that
400 are poleward of around 50° (such as central Asia). Supplemental Figure 2 shows strong sensitivity
401 of T_{max}^{2m} to the precipitation corrections across nearly all of the southern Hemisphere, including the
402 Amazon and tropical Africa. Since these latter two areas typically have saturated soils, this strong
403 signal is unlikely due to the precipitation-soil moisture pathway, and is perhaps due to sensitiv-
404 ity of evaporative cooling from the canopy interception to changes in precipitation supply to the
405 interception reservoir.

406 *c. Biases over Boreal summer*

407 In Section 3.a, the biases in the reanalyses' global land energy budgets were provided as annual
408 means. The seasonal cycle of the monthly mean global land biases (not shown) reveal that the
409 largest global land biases for all budget terms occur in the Boreal summer (JJA). Below, maps of
410 these JJA biases are presented and discussed, together with the corresponding biases in 2 m air
411 temperatures.

412 1) ENERGY BUDGET TERMS

413 Figure 4 shows maps of the reanalyses' JJA biases in LH and SH compared to each of GLEAM
414 and MTE. For LH, the regions of positive and negative biases relative to GLEAM or MTE are
415 similar (compare the first and second columns of Figure 4). For both, the LH biases depend on the
416 local LH regime, with energy-limited regions (low $R_{anom}^2(LH, SM)$ in Figure 2) generally having
417 larger positive LH biases ($> 20 \text{ W m}^{-2}$; e.g., for MERRA-2 in Figures 4d,e across the tropics, south
418 Asia, and the northern high latitudes), while moisture-limited regions (high $R_{anom}^2(LH, SM)$ in

419 Figure 2) tend to have smaller biases (magnitude $<10 W m^{-2}$). Consequently, the spatial correlation
420 between $R_{anom}^2(LH, SM)$ (as plotted in Figure 2) and the MERRA-2 LH biases is -0.65 for GLEAM
421 and -0.73 for MTE.

422 The MERRA LH biases (Figures 4j,k) show some of the same features as for MERRA-2, again
423 with a tendency for large positive biases in energy-limited LH regimes. The most prominent
424 difference is the sharp bias gradient in MERRA around $10^{\circ}S$ (most notable in South America).
425 As discussed in Section 2.b, this is associated with the unrealistically large rainfall interception
426 reservoir in MERRA, combined with the MERRA precipitation errors; these problems have been
427 alleviated in MERRA-2 (and MERRA-Land). Additionally, there are some isolated regions of
428 large positive biases in moisture-limited regimes in MERRA that are removed in MERRA-2 (and
429 MERRA-Land), such as in Mexico and south India.

430 Overall, in energy-limited regions ($R_{anom}^2(LH, SM) < 0.5$ in Figure 2) the area-averaged LH bias
431 in MERRA-2 ($25.5 W m^{-2}$ compared to GLEAM, $29.9 W m^{-2}$ compared to MTE) was slightly
432 higher than for MERRA ($24.1 W m^{-2}$ compared to GLEAM, $27.6 W m^{-2}$ compared to MTE), both
433 of which are much higher than for MERRA-Land ($11.3 W m^{-2}$ compared to GLEAM, and 7.6
434 $W m^{-2}$ compared to MTE). In contrast, in moisture-limited LH regions ($R_{anom}^2(LH, SM) > 0.5$ in
435 Figure 2), the area-averaged LH bias is highest in MERRA ($7.0 W m^{-2}$ compared to GLEAM,
436 $5.2 W m^{-2}$ compared to MTE), and reduced in MERRA-2 ($3.8 W m^{-2}$ compared to GLEAM, 1.5
437 $W m^{-2}$ compared to MTE), and even further reduced in MERRA-Land ($0.3 W m^{-2}$ compared to
438 GLEAM, $-2.9 W m^{-2}$ compared to MTE).

439 The third column of Figure 4 shows the reanalyses biases in SH compared to MTE. In gen-
440 eral, the SH biases for each reanalyses have an inverse relationship with the LH biases in the
441 first two columns (for MERRA-2, the spatial correlation between the SH biases and the LH bi-
442 ases is -0.68 for GLEAM LH and -0.78 for MTE LH). Consequently, the evaporative fraction

443 (EF=LH/(LH+SH)) biases compared to MTE in the first column of Figure 5 show a spatial pattern
444 very similar to that of the LH biases (for MERRA-2, the spatial correlation between MTE LH and
445 EF biases is 0.83).

446 The sum of LH and SH approximates the net incoming radiation (after neglecting the ground heat
447 flux and temporal change in T_{skin}). The second and third columns of Figure 5 show, respectively,
448 the biases in the reanalyses LH+SH sum compared to MTE and the biases in their R_{net} compared
449 to CERES-EBAF. There is a weak agreement between the R_{net} biases suggested by MTE and
450 CERES-EBAF (for MERRA-2, the spatial correlation is 0.46). Comparison to MTE (Figures 5,
451 second column) suggests that the reanalyses net surface radiation tends to be overestimated, with
452 the largest biases ($>30 Wm^{-2}$) occurring over the Amazon, the horn of Arica, and the Tibetan
453 Plateau. While comparison to CERES-EBAF (Figure 5, third column) also suggests relatively
454 large positive biases over the Tibetan Plateau and the horn of Africa, these positive biases are
455 smaller in both magnitude and regional extent than was suggested by MTE. Additionally, CERES-
456 EBAF also indicates strong negative biases ($<-30 Wm^{-2}$) over the Sahel and the southeast US,
457 particularly in MERRA-Land (Figure 5i) and MERRA (Figure 5l). Finally, inter-comparing the
458 R_{net} biases for each reanalyses shows qualitatively that the broad patterns are similar in MERRA-2
459 and MERRA (also MERRA-Land), although MERRA has a tendency towards larger (positive and
460 negative) biases.

461 There is no obvious correspondence between the regional biases in the LH (compared to
462 GLEAM or MTE) and the regional biases in R_{net} (compared to either MTE LH+SH or CERES-
463 EBAF). For example, the spatial correlations are less than 0.1 between the MERRA-2 LH bias
464 (implied by comparison to GLEAM or MTE), and the MERRA-2 LH+SH bias (implied by MTE).
465 Likewise, the spatial correlations are again less than 0.1 between the MERRA-2 LH bias (implied
466 by GLEAM or MTE) and the MERRA-2 R_{net} bias (implied by CERES-EBAF). This suggests then

467 that the pattern of regional biases in the reanalyses LH for JJA (compared to either GLEAM or
468 MTE) are associated with differences in the partitioning of incoming radiation into LH and SH,
469 rather than with differences in the surface radiation (compared to MTE or CERES-EBAF) itself.

470 While radiation biases do not appear to be the main predictor of LH biases, biased radiation will
471 results in biased LH and/or SH. Hence, we have partitioned the JJA R_{net} bias between MERRA-2
472 and CERES-EBAF into the individual contributions from each radiation term. Figure 6 shows the
473 JJA biases between MERRA-2 and CERES-EBAF for the SW_{net} , LW_d , and LW_u . In terms of the
474 direction of the biases, the broad patterns of regional biases in the radiation terms are unchanged
475 from MERRA (not shown). The direction of the regional R_{net} biases for MERRA-2 in Figure 5f
476 largely mirror the regional SW_{net} biases in Figure 6d (spatial correlation: 0.75), the main exception
477 being over the southeast US. The LW biases are somewhat balanced, in that both are negative
478 across most of the domain, with the LW_d bias in Figure 6e typically being slightly more negative
479 than the LW_u bias in Figure 6f. Both have relatively large negative biases (magnitude $> 30 Wm^{-2}$)
480 in northern hemisphere desert regions, and smaller (magnitude: 10-20 Wm^{-2}) negative biases
481 elsewhere. The spatial distribution of the SW_{net} biases mirrors that of the downwelling shortwave
482 (SW_d , not shown), indicating that the SW_{net} biases are primarily driven by SW_d differences rather
483 than differences in the surface albedo used in CERES-EBAF and GEOS-5. The above patterns
484 of overestimated SW_{net} (or SW_d) and underestimated LW_d across much of the globe are consistent
485 with a known tendency for the GEOS-5 systems to underestimate mid-latitude continental cloud
486 cover (Molod et al. 2012; Wang and Dickinson 2013; Gelaro and Coauthors 2015).

487 The LW_u is calculated from the T_{skin} , and the negative biases in MERRA-2 (and also MERRA
488 and MERRA-Land) indicate a cool bias in the model T_{skin} . At 285 K, a LW_u bias of 10 Wm^{-2} is
489 roughly equivalent to a T_{skin} bias of 2 K. Recall that the CERES-EBAF LW_u is not independent of
490 the MERRA suite of reanalyses, due to its use of GEOS-5 T_{skin} . However, the input GEOS-5 T_{skin}

491 is adjusted within the CERES-EBAF algorithm to constrain the TOA irradiance, so comparison
492 of GEOS-5 and CERES LW_u indicates the adjustment required to the GEOS-5 T_{skin} to balance the
493 TOA fluxes. Previous work has also suggested that the GEOS-5 T_{skin} is underestimated, partic-
494 ularly in dry regions. For example, in agreement with our Figure 6f, Draper et al. (2015) found
495 large cool biases in the GEOS-5 T_{skin} over desert regions in summer (their Fig. 5), compared to
496 remotely sensed observations. As argued in Draper et al. (2015), this GEOS-5 T_{skin} cool bias is,
497 at least in part, caused by the model's T_{skin} definition differing from that of a true skin layer from
498 which LW_u is emitted (or as is observed in the thermal infrared).

499 In summary, the pattern of regional LH biases in the reanalyses suggested by GLEAM and MTE
500 are very similar. This result adds confidence to the use of GLEAM and MTE for estimating re-
501 gional biases in the reanalyses. As with the annual global land averages in Figure 1, the maps
502 presented here suggest that MERRA-2 and MERRA (but not MERRA-Land) have a general ten-
503 dency to overestimate LH. If the GLEAM, MTE, and CERES-EBAF regional means are assumed
504 to be more accurate than the reanalyses, the above comparisons suggest that in energy-limited
505 regions, MERRA-2 (and MERRA) overestimate LH due to an overestimated evaporative fraction
506 (i.e., too much incoming radiation is converted to LH rather than SH). There is little change in the
507 global average biases from MERRA to MERRA-2. However, there are some isolated regions in
508 Mexico and south Asia that are typified by moisture-limited LH, where MERRA has positive LH
509 biases associated with overestimated EF, while MERRA-2 and MERRA-Land have much smaller
510 biases. The precipitation corrections in MERRA-2 (and MERRA-Land) removed a relatively large
511 amount of precipitation across these locations (Reichle et al. (2017b); their Figure 3b), strongly
512 suggesting that the use of precipitation observations in these products reduced the LH biases.

513 2) AIR TEMPERATURE

514 The biases in the MERRA-2 and MERRA JJA monthly mean daily minimum, daily maximum,
515 and diurnal range in T^{2m} , relative to the CRU data set, are shown in Figure 7 (T^{2m} is not calculated
516 by the land-only MERRA-Land system). For the daily minimum T^{2m} (T_{min}^{2m}) in the left column,
517 both reanalyses tend towards positive (warm) biases, particularly MERRA. For the daily maximum
518 T^{2m} (T_{max}^{2m}) in the center column, MERRA-2 tends towards cool biases, with patches of warm
519 biases across central Asia and the Arabian Peninsula (investigation of the large positive bias in
520 the Arabian Peninsula suggests it is associated with an error in the CRU reference data, rather
521 than the reanalyses). For MERRA, these patches of positive bias are expanded to cover most of
522 the desert region in the northern hemisphere, and also much of the southern hemisphere. For
523 the diurnal temperature range (DTR) in the third column, the MERRA-2 biases inherit the broad
524 spatial pattern of the T_{max}^{2m} biases, while for MERRA some of the large positive T_{max}^{2m} biases are
525 offset in the DTR by co-located positive T_{min}^{2m} .

526 The LH and SH biases in Figures 4 and the DTR biases in Figure 7 show some of the ex-
527 pected regional similarities. In particular, in the high latitudes and the Amazon MERRA-2 has
528 relatively large positive LH biases (and negative SH biases) and relatively large negative DTR bi-
529 ases. MERRA also has overestimated LH and underestimated DTR in the same regions, as well
530 as in southeast Asia and central America. This is consistent with an underestimated DTR caused
531 by underestimated SH (and overestimated LH), particularly given that the R_{net} bias is generally
532 neutral in these regions in Figure 5. It should however be noted that the high latitudes and the
533 Amazon regions are both data-scarce, and both the reanalyses and reference data sets are less well
534 constrained. In other regions there is less correspondence. For example the western US also has
535 underestimated DTR for MERRA and MERRA-2, while neither GLEAM nor MTE suggests over-

536 estimated LH. Over all, the spatial correlations between the LH biases and DTR biases are rather
537 low (for MERRA-2, they are -0.38 for GLEAM and -0.47 for MTE).

538 Recall that in Section 3.c.1 above, the CERES-EBAF comparison suggested that the MERRA-2
539 (and MERRA) T_{skin} is generally biased cool, with larger cool biases in desert areas. However, a
540 comparison of the LW_u biases in Figure 6f to the T_{min}^{2m} and T_{max}^{2m} biases in Figures 7d,e shows little
541 correspondence between them, and in particular the regions of relatively large cool T_{skin} biases
542 (underestimated LW_u) in the northern hemisphere deserts do not have cool biases in either T_{max}^{2m}
543 and T_{min}^{2m} . This apparent contradiction between the temperature biases suggested by comparison
544 to the CERES-EBAF LW_u ($\sim T_{skin}$) and the CRU T^{2m} does not necessarily imply that one of these
545 data sets is incorrect, given the likelihood mentioned above that the model T_{skin} biases are at least
546 partly associated with the model definition of T_{skin} .

547 *d. Turbulent heat flux anomaly correlations over Boreal summer*

548 Here the monthly mean turbulent heat flux time series are evaluated over Boreal summer based
549 on their temporal correlations (R_{anom}) with the reference data sets. Figure 8 shows maps of the
550 JJA R_{anom} for each of the NASA reanalyses (MERRA-2, MERRA-Land, and MERRA) and ERA-
551 Interim, with the R_{anom} calculated separately vs. each of the GLEAM and MTE turbulent heat
552 fluxes. For LH, the regional patterns in the R_{anom} vs. either GLEAM (Figure 8, first column) or
553 MTE (Figure 8, second column) show some similar features (for MERRA-2, spatial correlation
554 between Figures 8a and 8b: 0.69). Comparison to Figure 2 again suggests some dependence on
555 the LH regime. In the Northern Hemisphere, the LH R_{anom} is generally highest (~ 0.6) in regions
556 where LH is moisture-limited, and generally much lower (<0.2) where LH is energy-limited. The
557 two exceptions are the high latitudes, which have high LH R_{anom} and energy-limited LH, and the

558 Sahara, which has low LH R_{anom} and is moisture-limited (although LH variability in the Sahara is
559 very low, making the signal susceptible to noise).

560 The R_{anom} patterns for ERA-Interim in the final row of Figure 8 provide some additional context
561 for evaluating the NASA reanalyses. The LH R_{anom} values are generally higher for ERA-Interim
562 than for the NASA reanalyses. As for MERRA-2, the ERA-Interim R_{anom} vs MTE is relatively
563 low in many energy-limited LH regimes (including the eastern US, tropics, and south Asia), while
564 the R_{anom} for ERA-Interim vs. GLEAM is more spatially consistent, in contrast to the R_{anom} for
565 MERRA-2. The relatively high R_{anom} between GLEAM and ERA-Interim LH in energy-limited
566 LH regimes may well be due to GLEAM having used ERA-Interim radiation and temperature,
567 since it is in these regions that these fields will have the strongest influence on the LH. On the
568 other hand, the lower R_{anom} between the NASA reanalyses and the LH reference data sets (and
569 also between ERA-Interim and MTE) could be attributed to errors in both the reference data sets
570 and the reanalyses under energy-limited conditions. For MTE, this result was expected because
571 MTE is thought to be more reliable in estimating temporal variability in moisture limited areas,
572 since its temporal variability is largely driven by fPAR (Jung et al. 2010).

573 Moving on to SH, the third column of Figure 8 shows the R_{anom} vs. MTE for each reanalysis.
574 The regional patterns are similar to those for LH, with higher R_{anom} (>0.5) in moisture-limited
575 LH regions, and lower (< 0.2) values elsewhere. ERA-Interim R_{anom} vs. MTE is generally higher
576 than the NASA reanalyses, with values greater than 0.5 across most of the globe (and particularly
577 in the Northern Hemisphere). Despite the improved LH from MERRA-Land, the SH R_{anom} vs.
578 MTE is lower than for MERRA (or MERRA-2).

579 Globally averaged, the rank order of the mean LH R_{anom} , while rather low, is the same vs. ei-
580 ther GLEAM or MTE and follows the expected progression of improvement from MERRA, to
581 MERRA-Land, and then to MERRA-2. GLEAM suggests a larger improvement, from a globally

582 averaged R_{anom} of 0.39 for MERRA to 0.48 for MERRA-2, with MERRA-Land falling in be-
583 tween (0.45). MTE suggests an improvement from 0.29 for MERRA to 0.34 for MERRA-2, with
584 MERRA-Land again falling in between (0.32). For SH, the globally averaged R_{anom} vs. MTE is
585 similar for MERRA (0.36) and MERRA-2 (0.37), but is much lower for MERRA-Land (0.28). For
586 ERA-Interim, the global mean R_{anom} for LH is ~ 0.1 higher than for MERRA-2 (0.60 vs. GLEAM,
587 and 0.44 vs. MTE) and ~ 0.2 higher for SH (0.46 vs. MTE). The better agreement between ERA-
588 Interim and the reference data sets could be a consequence of the land surface updates applied in
589 ERA-Interim, which indirectly targets the turbulent heat fluxes. (Although recall that the relatively
590 strong agreement between the GLEAM and ERA-Interim LH will partly reflect their dependence;
591 see Section 2.c.2).

592 *e. Comparison to Fluxnet tower data*

593 Since the reference data sets used above do not represent direct observations, we now com-
594 pare the globally-averaged LH and SH statistics from Section 3.a (for the annual mean turbulent
595 heat fluxes over land), and Section 3.d (for the mean JJA R_{anom}) to statistics calculated against
596 Fluxnet-2015 tower observations. Figure 9 shows the annual mean of the turbulent fluxes aver-
597 aged across the 20 tower sites for the Fluxnet (eddy-covariance) measurements themselves and for
598 each reanalysis and reference data set averaged across the 20 Fluxnet locations, with the global
599 land annual means (from Figure 1) included for reference. For LH, comparison to the Fluxnet
600 observations agrees with the results from the global land comparison in Section 3.a, again sug-
601 gesting that the MERRA-2 LH is biased high, although the Fluxnet observations suggest a larger
602 bias (of 12 Wm^{-2} , or 30%) than was suggested by the global comparison (estimated as 6 Wm^{-2}
603 in Section 3.a). Averaged across the 20 Fluxnet sites, the MTE LH is very close to the Fluxnet
604 data (within 0.5 Wm^{-2}), while GLEAM is slightly higher. For the interested reader, supplemental

605 Figure 3 shows scatterplots comparing the MERRA-2 and reference data set LH annual means at
606 the 20 individual sites.

607 For SH, the Fluxnet observations agree less well with the global land comparison. First, the
608 annual mean of the Fluxnet data is about 10 Wm^{-2} below the global mean estimates from the
609 other reference data sets. For each of the global reference data sets and reanalyses, the annual
610 average over the 20 Fluxnet sites is also $15\text{-}20 \text{ Wm}^{-2}$ lower than the global average, suggesting
611 that the relatively low Fluxnet annual mean is associated with the spatial sampling of the Fluxnet
612 sites. Second, averaged across the Fluxnet sites, the Fluxnet mean SH is close to that of MERRA-
613 Land, and above that of MERRA-2 (by 6 Wm^{-2} , 18 %). In contrast, for the global averages in
614 Section 3.a the reference data sets were all close to MERRA-2 (and MERRA), with MERRA-Land
615 standing out as being biased high.

616 Figure 10 shows the JJA R_{anom} averaged over the 20 Fluxnet sites for each reanalyses vs. each of
617 Fluxnet, GLEAM, and MTE, with the global average JJA R_{anom} from Section 3.d also included for
618 GLEAM and MTE. The R_{anom} for the Fluxnet data are quite low, which is somewhat expected due
619 to the mismatch in spatial representation between the tower-based observations and the reanalysis.
620 Nonetheless, the Fluxnet R_{anom} (as well as the GLEAM and MTE R_{anom} at the same locations)
621 indicates similar relative reanalysis performance as the global mean R_{anom} . In particular, for LH
622 MERRA-2 and MERRA-Land outperform MERRA, as also indicated by the global means. How-
623 ever, the one discrepancy is that the R_{anom} vs. the Fluxnet data is similar for ERA-Interim and
624 MERRA-2, while the global comparisons (and also the GLEAM and MTE data averaged across
625 the Fluxnet sites) all suggest that ERA-Interim outperforms MERRA-2 (giving mean R_{anom} around
626 0.1 higher). For SH, the rank order between the average JJA R_{anom} is the same from the Fluxnet
627 data than from the global reference data sets, with the MERRA-Land R_{anom} again being lower than

628 that for MERRA (and MERRA-2), and the ERA-Interim average R_{anom} being higher than that for
629 MERRA-2.

630 It is notable that over the Fluxnet tower sites, both GLEAM and MTE have higher average R_{anom}
631 with the reanalyses than the Fluxnet observations do. In particular, MTE was trained on an earlier
632 generation of the Fluxnet data, and the higher mean R_{anom} vs. MTE than vs. Fluxnet suggests that
633 the MTE algorithm has added coarse-scale information (similar quality control was applied here
634 as was applied to the tower observations used in MTE). For the interested reader, supplemental
635 Figure 4 shows scatterplots of the MERRA-2 LH R_{anom} vs. each reference data set at the 20
636 individual sites.

637 Note that for Fluxnet, the R_{anom} for (LH+SH), plotted in Figure 10c is consistently about 0.1
638 higher than the R_{anom} for either LH or SH separately. Decker et al. (2012) obtained a similar
639 result for the correlation between reanalyses and tower observations. This indicates that the eddy
640 covariance measurements and the reanalyses have a stronger agreement in the implied incoming
641 radiation than in the partitioning of that radiation into LH and SH (this result is unchanged if the
642 R_{anom} are calculated from the Fluxnet data that have not been energy balance-corrected). This
643 could be a signal of errors in the partitioning within the reanalyses, or perhaps just as likely,
644 this difference is associated with the spatial representation of the tower observations, since the
645 incoming radiation is more spatially homogeneous than either LH or SH on its own.

646 *f. Precipitation Corrections and Air Temperature Performance*

647 Finally, we seek to establish whether the precipitation corrections in MERRA-2 influenced the
648 local T_{max}^{2m} . We do this by comparing the performance of the MERRA-2 and MERRA T_{max}^{2m} to
649 Figure 3c, which shows the MERRA-2 sensitivity to observed precipitation. Figure 11 shows the
650 $T_{max}^{2m} R_{anom}$ vs. CRU observations over JJA for MERRA-2 and MERRA. In general, the MERRA-

651 $2 R_{anom}$ is high (> 0.7) across most of the domain, particularly in the high latitudes, with much
652 lower (< 0.4) values across much of the tropics and parts of South America, Africa, and south
653 Asia. Note that the latter regions all have relatively sparsely distributed CRU station data, which is
654 likely contributing to the lower agreement with the reanalyses. Compared to MERRA, the greatest
655 improvements in the MERRA-2 $T_{max}^{2m} R_{anom}$ occurred in the eastern US, much of tropical South
656 America and Africa, the Sahel, and parts of south Asia and China. There are also several regions
657 where the $T_{max}^{2m} R_{anom}$ is reduced, including northern South America, and much of southeast Asia.
658 Overall, the global averaged $T_{max}^{2m} R_{anom}$ vs. CRU was increased from 0.69 for MERRA to 0.75 for
659 MERRA-2.

660 Comparing Figure 11c to Figure 3c, the regions with the strongest sensitivity of T_{max}^{2m} to the
661 precipitation corrections generally have relatively large changes in the $T_{max}^{2m} R_{anom}$ (including the
662 Sahel, parts of south Asia, and central America). Consequently, where the metric in Figure
663 3c is above 0.25 (i.e., the observation-corrected precipitation explains at least 25% more of the
664 MERRA-2 T_{max}^{2m} variance than the model-generated precipitation does), the area-averaged absolute
665 change in the R_{anom} is 0.15, compared to an area-average absolute change of 0.07 elsewhere. This
666 tendency toward relatively large change in the $T_{max}^{2m} R_{anom}$ where T_{max}^{2m} is sensitive to the precipita-
667 tion corrections suggests that the observed precipitation in MERRA-2 contributed to the change in
668 T_{max}^{2m} performance. Additionally, the change in $T_{max}^{2m} R_{anom}$ in these regions is generally, although
669 not always, positive (giving an area averaged change in the R_{anom} of 0.06 where the metric in Fig-
670 ure 3c is greater than 0.25). In some of the instances where the $T_{max}^{2m} R_{anom}$ is degraded, this can be
671 traced back to errors in the precipitation observation data sets input into MERRA-2. For example,
672 over Myanmar, the $T_{max}^{2m} R_{anom}$ is decreased by more than 0.15, likely due to persistent local errors
673 in the precipitation observations input into MERRA-2 (Reichle et al. 2017b). Finally, there are
674 also regions with large changes in the $T_{max}^{2m} R_{anom}$ outside of the regions of T_{max}^{2m} sensitivity to pre-

675 cipation (the eastern US, tropical Africa and South America, and central China). The $T_{max}^{2m} R_{anom}$
676 is increased in MERRA-2 across most of these regions, likely due to other advances (beyond the
677 use of observed precipitation) in the MERRA-2 modeling and assimilation system.

678 **4. Summary and conclusions**

679 The land surface energy budgets of three reanalyses from NASA (MERRA, MERRA-Land, and
680 MERRA-2) are compared here to the best available estimates from the literature and to (largely)
681 independent global reference data sets. In terms of the global land annual averages, the results sug-
682 gest that the MERRA-2 LH and SH are biased high by $5 Wm^{-2}$ and $6 Wm^{-2}$, respectively, while
683 SW_u has a large positive bias of $14 Wm^{-2}$, SW_d is biased high by $3 Wm^{-2}$, and the upwelling and
684 downwelling LW components are biased low, by $11 Wm^{-2}$ and $13 Wm^{-2}$, respectively. Compared
685 to MERRA, this is a slight ($\sim 2 Wm^{-2}$) reduction in the LH and SW_{net} biases, while the difference
686 is even smaller for the LW terms ($\sim 1 Wm^{-2}$). The radiation biases are associated with known
687 issues in the GEOS-5 models used in the reanalyses, specifically a tendency to underestimate mid-
688 latitude continental clouds (Wang and Dickinson 2013) and a cool bias in the model T_{skin} (Draper
689 et al. 2015).

690 Compared to reference flux estimates from GLEAM and MTE over the Boreal summer (when
691 both the fluxes themselves and their biases are greatest), the largest MERRA-2 LH biases (>20
692 Wm^{-2} , vs. either GLEAM or MTE) occur in regions where LH is energy-limited, such as in the
693 high latitudes, the tropics, parts of south Asia, and the eastern US. The MERRA-2 LH biases are
694 typically smaller in regions where LH is moisture-limited, which include the drier regions of the
695 mid and low latitudes. In some of these moisture-limited regions (parts of south Asia and Mexico)
696 the high bias in the MERRA LH was largely removed in MERRA-2 (and MERRA-Land), likely
697 because the observed precipitation used in the latter was lower than that produced by the MERRA

698 (or MERRA-2) modeling systems. Finally, comparison to the evaporative fraction from MTE and
699 to R_{net} from CERES-EBAF or as inferred from MTE LH+SH indicates that the regional biases in
700 the reanalyses LH are generally associated with differences in the partitioning of R_{net} into LH and
701 SH rather than with differences in the radiation input.

702 The temporal agreement between the reanalyses and the reference data sets over Boreal summer
703 was measured using the monthly anomaly correlation (R_{anom}) over JJA. For LH, the R_{anom} between
704 the reanalyses and the reference data sets (GLEAM and MTE) again showed some dependency
705 on the LH regime, with a tendency towards better agreement where LH is moisture-limited than
706 where it is energy-limited. The lower agreement in energy-limited regions does not necessar-
707 ily imply poorer performance in the reanalyses, as it may be due to errors in the reference data
708 sets. The globally averaged R_{anom} values show the expected improvement in skill with each new
709 NASA reanalyses. For example, MERRA-2 has slightly better globally averaged LH R_{anom} (0.48
710 vs GLEAM) than MERRA-Land (0.45), which is substantially better than MERRA (0.39). The
711 R_{anom} was also calculated for the monthly mean daily T_{max}^{2m} vs. CRU reference data over JJA. Av-
712 eraged over global land, the JJA T_{max}^{2m} R_{anom} vs. CRU increased from 0.69 for MERRA to 0.75
713 for MERRA-2. The results presented above for the regional biases and R_{anom} were based on the
714 Boreal summer, however the same analysis has been performed over the Austral summer (not
715 shown), yielding qualitatively similar results.

716 The use of observed precipitation in MERRA-2 was motivated by the hope that the subsequent
717 improvements in simulated soil moisture would lead to the improved partitioning of incoming
718 radiation between latent and sensible heating, ultimately leading to improvements in the diurnal
719 evolution of the boundary layer. It is difficult, however, to unequivocally attribute the improve-
720 ments in MERRA-2 to the use of observed precipitation because MERRA-2 includes many other
721 modeling and assimilation advances relative to MERRA. Nonetheless, many of the improvements

722 in the MERRA-2 LH and T^{2m} are consistent with the changes expected from the use of observed
723 precipitation. MERRA-2 and MERRA-Land have smaller positive LH biases and higher LH R_{anom}
724 than MERRA in regions where LH is moisture-limited and thus sensitive to precipitation (south
725 Asia and the western US). This is most easily explained by the forcing of the land surface with ob-
726 served precipitation in MERRA-2. Additionally, regions where the MERRA-2 JJA T_{max}^{2m} was most
727 sensitive to the precipitation corrections (the Sahel, central US, and parts of south Asia), generally
728 experience larger changes in the $T_{max}^{2m} R_{anom}$ from MERRA to MERRA-2. However, the changes
729 in R_{anom} in these areas are not uniformly positive, and in some cases degraded $T_{max}^{2m} R_{anom}$ can be
730 traced back to problems in the input precipitation data sets (e.g., over Myanmar). In the future, the
731 use of precipitation corrections could be enhanced by also implementing a land data assimilation
732 scheme to update the model soil moisture according to observations (e.g., Draper et al. (2011);
733 Dharssi et al. (2011); De Lannoy and Reichle (2016)). By making use of remotely sensed obser-
734 vations, the land data assimilation would be particularly valuable in regions where the rain-gauge
735 network is sparse or has known problems (e.g., in Africa and parts of southeast Asia).

736 However, some of the largest biases and lowest R_{anom} for the MERRA-2 turbulent fluxes occur
737 where the LH is energy-limited and thus less sensitive to improvements in the precipitation and
738 soil moisture. Hence, future efforts to improve the MERRA-2 land surface turbulent fluxes would
739 best be focused on other facets of the modeling and assimilation. Specifically, future GEOS-5
740 development should focus on the overestimated evaporative fraction where LH is energy-limited.
741 Additionally, even though the MERRA-2 R_{net} is relatively unbiased (compared to CERES-EBAF),
742 there are large compensating biases in the individual SW and LW radiation fluxes that are 2-3 times
743 the magnitude of the LH biases in terms of the global land annual averages. Reducing the cloud
744 bias in the atmospheric model will help these biases, as will re-defining the model T_{skin} to generate
745 a LW_u more consistent with observations.

746 Finally, the SH results for MERRA-Land are troubling. While MERRA-Land did have the
747 desired reduction in the LH biases compared to MERRA (to 1 Wm^{-2} in the global land annual
748 average), it also had a compensating, and much larger, increase in the SH bias (up to 15 Wm^{-2}
749 in the global land average). Additionally, the JJA R_{anom} compared to MTE were reduced from
750 MERRA to MERRA-Land (from a global average of 0.36 to 0.28), despite the LH R_{anom} being
751 increased. The cause of the degraded SH in MERRA-Land is presently unknown, but given the
752 otherwise similar MERRA and MERRA-Land land surface models and meteorological forcing,
753 an obvious possibility is that the use of observed precipitation in an offline (land-only) replay of
754 an analysis, such as MERRA-Land, can lead to inconsistencies in the forcing (e.g., warm and dry
755 air, stemming from dry conditions in MERRA, overlying cold ground induced by high antecedent
756 rainfall from the observations). Such inconsistencies would not appear in MERRA or (as much)
757 in MERRA-2, given the coupling in the reanalyses of the land surface state with the overlying
758 atmosphere.

759 While this work focused on evaluating surface energy fluxes in MERRA-2, the findings have
760 relevance to anyone interested in designing a methodology to evaluate global estimates of turbu-
761 lent heat fluxes. The gridded LH reference data sets (GLEAM and MTE) had better agreement
762 with the reanalyses time series (as measured by R_{anom}), and were more useful for evaluating the
763 reanalysis output than were the tower observations. In particular they offer (near-) global cover-
764 age across several decades, at similarly coarse resolution to the reanalyses. In the absence of a
765 recognized truth for LH (or other similar terms), the recommended evaluation strategy is to com-
766 pare the product under evaluation to multiple data sets. However, given the uncertainty in the
767 available reference data sets, extra care is necessary to understand the methodology, input data,
768 assumptions, and potential dependencies and weaknesses of each reference data set. This process
769 relies on expert judgement and inevitably introduces some subjectivity into the interpretation of

770 the results. Further development of global gridded LH data sets (including the quality and quantity
771 of ground-‘truth’ observations), to increase their confidence would obviously be of great benefit
772 to this process.

773 The GLEAM and MTE reference data sets used here are independent of each other and are based
774 on very different methodologies, thus providing complementary information for use in an evalua-
775 tion. However, given the use of the common precipitation input data in GLEAM as in MERRA-2,
776 and the fact that MTE data is not optimized to estimate interannual variability, LH estimates from
777 a third reference data set would be useful. Emerging global and multi-decadal land surface flux
778 data sets based on an energy balance approach (Anderson et al. 2011), or alternative observational
779 frameworks (Alemohammad et al. 2017) would provide useful complements to GLEAM and MTE
780 for a more comprehensive analysis.

781 *Acknowledgments.* Funding for this work was provided by the NASA Modeling, Analysis, and
782 Prediction program. Computational resources were provided by the NASA High-End Computing
783 Program through the NASA Center for Climate Simulation. The authors acknowledge the teams
784 that produce and publish the GLEAM, MTE, CERES-EBAF, ERA-Interim, MERRA, MERRA-
785 Land, and MERRA-2 products. Additionally, we are grateful to Diego Miralles (VU University
786 Amsterdam/Ghent University), Martin Jung (Max Planck Institute for Biogeochemistry), and Seiji
787 Kato (NASA Langley Research Center) for their thoughtful feedback on this work, and detailed
788 advice on the use of GLEAM, MTE, and CERES-EBAF, respectively. The FLUXNET eddy co-
789 variance data processing and harmonization was carried out by the European Fluxes Database
790 Cluster, AmeriFlux Management Project, and Fluxdata project of FLUXNET, with the support of
791 CDIAC and ICOS Ecosystem Thematic Center, and the OzFlux, ChinaFlux and AsiaFlux offices.

792 **References**

- 793 Alemohammad, S. H., and Coauthors, 2016: Water, Energy, and Carbon with Artificial Neural
794 Networks (WECANN): A statistically-based estimate of global surface turbulent fluxes using
795 solar-induced fluorescence. *Biogeosciences*, **15**, 4101–4124, doi:10.5194/bg-14-4101-2017.
- 796 Anderson, M., and Coauthors, 2011: Mapping daily evapotranspiration at field to continental
797 scales using geostationary and polar orbiting satellite imagery. *Hydrology and Earth System
798 Sciences*, **15**, 223–239, doi:10.5194/hess-15-223-2011.
- 799 Baldocchi, D., and Coauthors, 2001: FLUXNET: A new tool to study the temporal and spatial
800 variability of ecosystem-scale carbon dioxide, water vapor, and energy flux densities. *Bulletin of
801 the American Meteorological Society*, **82**, 2415–2434, doi:10.1175/1520-0477(2001)082<2415:
802 FANTTS>2.3.CO;2.
- 803 Beck, H., A. van Dijk, V. Levizzani, J. Schellekens, D. Miralles, B. Martens, and A. de Roo,
804 2017: MSWEP: 3-hourly 0.25° global gridded precipitation (1979–2015) by merging gauge,
805 satellite, and reanalysis data. *Hydrology and Earth System Sciences*, **21**, 589–615, doi:10.5194/
806 hess-21-589-2017.
- 807 Betts, A., A. Tawfik, and R. Desjardins, 2017: Revisiting hydrometeorology using cloud and cli-
808 mate observations. *Journal of Hydrometeorology*, **18**, 939–955, doi:10.1175/JHM-D-16-0203.
809 1.
- 810 CERES-EBAF, 2017: CERES_EBAF-Surface_Ed4.0, Data Quality Summary (May 26, 2017). Ac-
811 cessed Jun. 20, 2017 pp., [https://ceres.larc.nasa.gov/documents/DQ_summaries/CERES_EBAF-](https://ceres.larc.nasa.gov/documents/DQ_summaries/CERES_EBAF-Surface_Ed4.0_DQS.pdf)
812 [Surface_Ed4.0_DQS.pdf](https://ceres.larc.nasa.gov/documents/DQ_summaries/CERES_EBAF-Surface_Ed4.0_DQS.pdf).

813 Chen, M., W. Shi, P. Xie, V. B. S. Silva, V. E. Kousky, R. Wayne Higgins, and J. E. Janowiak,
814 2008: Assessing objective techniques for gauge-based analyses of global daily precipitation.
815 *Journal of Geophysical Research: Atmospheres*, **113**, D04 110, doi:10.1029/2007JD009132.

816 De Lannoy, G., and R. Reichle, 2016: Assimilation of SMOS brightness temperatures or soil
817 moisture retrievals into a land surface model. *Hydrology and Earth System Sciences*, **20**, 4895–
818 4911, doi:10.5194/hess-20-4895-2016.

819 de Rosnay, P., G. Balsamo, C. Albergel, J. Munoz-Sabater, and L. Isaksen, 2014: Initialisation of
820 land surface variables for numerical weather prediction. *Surveys in Geophysics*, **35**, 607–621,
821 doi:10.1007/s10712-012-9207-x.

822 Decker, M., M. Brunke, Z. Wang, K. Sakaguchi, X. Zeng, and M. Bosilovich, 2012: Evaluation
823 of the Reanalysis Products from GSFC, NCEP, and ECMWF Using Flux Tower Observations.
824 *Journal of Climate*, **25**, 1916–1944, doi:10.1175/JCLI-D-11-00004.1.

825 Dee, D., and Coauthors, 2011: The ERA-Interim reanalysis: configuration and performance of the
826 data assimilation system. *Quarterly Journal of the Royal Meteorological Society*, **137**, 553–597,
827 doi:10.1002/qj.828.

828 Dharssi, I., K. Bovis, B. Macpherson, and C. Jones, 2011: Operational assimilation of ASCAT
829 surface soil wetness at the Met Office. *Hydrology and Earth System Sciences*, **15**, 2729–2746,
830 doi:0.5194/hess-15-2729-2011.

831 Draper, C., J.-F. Mahfouf, and J. Walker, 2011: Root-zone soil moisture from the assimilation
832 of screen-level variables and remotely sensed soil moisture. *Journal of Geophysical Research*,
833 **116**, D02 127, doi:10.1029/2010JD013829.

834 Draper, C., R. Reichle, and B. De Lannoy, G. and Scarino, 2015: A Dynamic Approach to Ad-
835 dressing Observation-Minus-Forecast Bias in a Land Surface Skin Temperature Data Assimila-
836 tion System. *Journal of Hydrometeorology*, **16**, 449–464, doi:10.1175/JHM-D-14-0087.1.

837 Fluxnet, 2015: FLUXNET2015 Dataset. Accessed Aug 9, 2016 pp.,
838 <http://fluxnet.fluxdata.org/data/fluxnet2015-dataset/>.

839 Gelaro, R., and Coauthors, 2015: Evaluation of the 7-km GEOS-5 Nature Run. 285pp pp., NASA
840 Technical Report Series on Global Modeling and Data Assimilation, NASA/TM-2014-104606,
841 Vol. 36.

842 Gelaro, R., and Coauthors, 2017: The Modern-Era Retrospective Analysis for Research and
843 Applications, Version 2 (MERRA-2). *Journal of Climate*, **30**, 5419–5454, doi:10.1175/
844 JCLI-D-16-0758.1.

845 Global Modeling and Assimilation Office, 2008a: tavg1_2d_slv_Nx: MERRA 2D IAU Diagnostic,
846 Single Level Meteorology, Time Average 1-hourly V5.2.0. Goddard Earth Sciences Data and
847 Information Services Center (GES DISC), Greenbelt, MD, Accessed Oct 1, 2016 pp., doi:10.
848 5067/B6DQZQLSFDLH.

849 Global Modeling and Assimilation Office, 2008b: tavgM_2d_lnd_Nx: MERRA 2D IAU Diagnos-
850 tic, Land Only States and Diagnostics, Monthly Mean V5.2.0. Goddard Earth Sciences Data
851 and Information Services Center (GES DISC), Greenbelt, MD, Accessed Oct 1, 2016 pp., doi:
852 10.5067/XOHTTIK0W9RK.

853 Global Modeling and Assimilation Office, 2008c: tavgM_2d_mld_Nx: MERRA Simulated 2D
854 Incremental Analysis Update (IAU) MERRA-Land reanalysis, GEOSldas-MERRALand, Time

855 Average Monthly Mean V5.2.0. Goddard Earth Sciences Data and Information Services Center
856 (GES DISC), Greenbelt, MD, Accessed Oct 1, 2016 pp., doi:10.5067/K9PCGOMQ1XP1.

857 Global Modeling and Assimilation Office, 2015a: MERRA-2 tavg1_2d_lfo_Nx: 2D, 1-Hourly,
858 Time-Averaged, Single-Level, Assimilation, Land Surface Forcings, V5.12.4. Goddard Earth
859 Sciences Data and Information Services Center (GES DISC), Greenbelt, MD, Accessed Oct 1,
860 2016 pp., doi:10.5067/L0T5GEG1NYFA.

861 Global Modeling and Assimilation Office, 2015b: MERRA-2 tavgM_2d_lnd_Nx: 2D, Monthly
862 Mean, Time-Averaged, Single-Level, Assimilation, Land Surface Diagnostics, V5.12.4. God-
863 dard Earth Sciences Data and Information Services Center (GES DISC), Greenbelt, MD, Ac-
864 cessed Oct 1, 2016 pp., doi:10.5067/8S35XF81C28F.

865 Global Modeling and Assimilation Office, 2015c: MERRA-2 tavgM_2d_slv_Nx: 2D, Monthly
866 Mean, Time-Averaged, Single-Level, Assimilation, Single-Level Diagnostics, V5.12.4. God-
867 dard Earth Sciences Data and Information Services Center (GES DISC), Greenbelt, MD, Ac-
868 cessed Oct 1, 2016 pp., doi:10.5067/AP1B0BA5PD2K.

869 Harris, I., P. Jones, T. Osborn, and D. Lister, 2014: Updated high-resolution grids of monthly
870 climatic observations - the CRU TS3.10 Dataset. *International Journal of Climatology*, **34**,
871 623642, doi:10.1002/joc.3711.

872 Huffman, G., R. Adler, D. Bolvin, and G. Gu, 2009: Improving the global precipitation
873 record: GPCP Version 2.1. *Geophysical Research Letters*, **36** (17), L17 808, doi:10.1029/
874 2009GL040000.

875 Jiménez, C., and Coauthors, 2011: Global intercomparison of 12 land surface heat flux estimates.
876 *Journal of Geophysical Research: Atmospheres*, **116**, D02 102, doi:10.1029/2010JD014545.

- 877 Jung, M., M. Reichstein, and A. Bondeau, 2009: Towards global empirical upscaling of
878 FLUXNET eddy covariance observations: validation of a model tree ensemble approach us-
879 ing a biosphere model. *Biogeosciences*, **6**, 2001–2013, doi:10.5194/bg-6-2001-2009.
- 880 Jung, M., and Coauthors, 2010: Recent decline in the global land evapotranspiration trend due to
881 limited moisture supply. *Nature*, **467**, 951–954, doi:10.1038/nature09396.
- 882 Jung, M., and Coauthors, 2011: Global patterns of land-atmosphere fluxes of carbon diox-
883 ide, latent heat, and sensible heat derived from eddy covariance, satellite, and meteoro-
884 logical observations. *Journal of Geophysical Research - Biogeosciences*, **116**, G00j07, doi:
885 10.1029/2010jg001566.
- 886 Kato, S., N. Loeb, F. Rose, D. Doelling, D. Rutan, T. Caldwell, L. Yu, and R. Weller, 2013: Surface
887 Irradiances Consistent with CERES-Derived Top-of-Atmosphere Shortwave and Longwave Ir-
888 radiances. *Journal of Climate*, **26**, 2719–2740, doi:10.1175/JCLI-D-12-00436.1.
- 889 Koster, R., G. Salvucci, A. Rigden, M. Jung, G. Collatz, and S. Schubert, 2015: The pattern across
890 the continental United States of evapotranspiration variability associated with water availability.
891 *Frontiers in Earth Science*, **3**, 35pp, doi:10.3389/feart.2015.00035.
- 892 Koster, R., and Coauthors, 2006: GLACE: The Global Land-Atmosphere Coupling Experiment.
893 Part I: Overview. *Journal of Hydrometeorology*, **7**, 590–610, doi:10.1175/JHM510.1.
- 894 L'Ecuyer, T., and Coauthors, 2015: The observed state of the Energy budget in the early 21st
895 Century. *Journal of Climate*, **28**, 8319–8346, doi:10.1175/JCLI-D-14-00556.1.
- 896 Martens, B., and Coauthors, 2017: GLEAM v3: satellite-based land evaporation and root-zone soil
897 moisture. *Geoscientific Model Development*, **10**, 1903–1925, doi:10.5194/gmd-10-1903-2017.

898 Miralles, D., T. Holmes, R. de Jeu, J. Gash, A. Meesters, and A. Dolman, 2011: Global land-
899 surface evaporation estimated from satellite-based observations. *Hydrology and Earth System*
900 *Sciences*, **15**, 453–469, doi:10.5194/hess-15-453-2011.

901 Miralles, D., M. van den Berg, A. Teuling, and R. de Jeu, 2012: Soil moisture-temperature cou-
902 pling: A multiscale observational analysis. *Geophysical Research Letters*, **39**, L21 707, doi:
903 10.1029/2012GL053703.

904 Molod, A., L. Takacs, M. Suarez, and J. Bacmeister, 2015: Development of the GEOS-5 atmo-
905 spheric general circulation model: evolution from MERRA to MERRA-2. *Geoscientific Model*
906 *Development*, **8**, 1339–1356, doi:10.5194/gmd-8-1339-2015.

907 Molod, A., L. Takacs, M. Suarez, J. Bacmeister, I.-S. Song, and A. Eichmann, 2012: The GEOS-5
908 atmospheric general circulation model: Mean climate and development from MERRA to For-
909 tuna . 117pp pp., NASA Technical Report Series on Global Modeling and Data Assimilation,
910 NASA/TM-2014-104606, Vol. 28.

911 Mueller, B., and Coauthors, 2011: Evaluation of global observations-based evapotranspiration
912 datasets and IPCC AR4 simulations. *Geophysical Research Letters*, **38**, L06 402, doi:10.1029/
913 2010GL046230.

914 Mueller, B., and Coauthors, 2013: Benchmark products for land evapotranspiration: LandFlux-
915 EVAL multi-data set synthesis. *Hydrology and Earth System Sciences*, **17**, 3707–3720, doi:
916 10.5194/hess-17-3707-2013.

917 NSIT, 2007: A NASA Earth science implementation plan for energy and water cycle research:
918 Predicting energy and water cycle consequences of Earth system variability and change. 89pp
919 pp., http://news.cisc.gmu.edu/doc/NEWS_implementation.pdf.

920 Reichle, R., C. Draper, Q. Liu, M. Girotto, S. Mahanama, R. Koster, and G. D. Lannoy, 2017a:
921 Assessment of MERRA-2 land surface hydrology estimates. *Journal of Climate*, **30**, 2937–2960,
922 doi:10.1175/JCLI-D-16-0720.1.

923 Reichle, R., R. Koster, G. De Lannoy, B. Forman, Q. Liu, S. Mahanama, and A. Toure, 2011:
924 Assessment and enhancement of MERRA land surface hydrology estimates. *Journal of Climate*,
925 **24**, 6322–6338, doi:10.1175/JCLI-D-10-05033.1.

926 Reichle, R., and Q. Liu, 2014: Observation-corrected precipitation estimates in GEOS-5. 18pp
927 pp., NASA Technical Report Series on Global Modeling and Data Assimilation, NASA/TM-
928 2014-104606, Vol. 35.

929 Reichle, R., Q. Liu, R. Koster, C. Draper, S. Mahanama, and G. Partyka, 2017b: Land surface
930 precipitation in MERRA-2. *Journal of Climate*, **30**, 1643–1664, doi:10.1175/JCLI-D-16-0570.
931 1.

932 Rienecker, M., and Coauthors, 2011: MERRA - NASA's Modern-Era Retrospective Analysis for
933 Research and Applications. *Journal of Climate*, **24**, 3624–3648, doi:10.1175/JCLI-D-11-00015.
934 1.

935 Schlosser, C., and X. Gao, 2010: Assessing evapotranspiration estimates from the Second Global
936 Soil Wetness Project (GSWP-2) simulations. *Journal of Hydrometeorology*, **11**, 880–897, doi:
937 10.1175/2010JHM1203.1.

938 Trenberth, K., J. Fasullo, and J. Kiehl, 2009: Earth's global energy budget. *Bulletin of the Ameri-
939 can Meteorological Society*, **90**, 311–323, doi:10.1175/2008BAMS2634.1.

940 University of East Anglia Climatic Research Unit, Harris I, and Jones, P, 2014: CRU TS3.22:
941 Climatic Research Unit (CRU) Time-Series (TS) Version 3.22 of High Resolution Gridded Data

942 of Month-by-month Variation in Climate (Jan. 1901- Dec. 2013). NCAS British Atmospheric
943 Data Centre, doi:10.5285/18BE23F8-D252-482D-8AF9-5D6A2D40990C.

944 Wang, K., and R. Dickinson, 2013: Global atmospheric downward longwave radiation at the
945 surface from ground-based observations, satellite retrievals, and reanalyses. *Reviews of Geo-*
946 *physics*, **51**, 150–185, doi:10.1002/rog.20009.

947 Wild, M., D. Folini, and M. Hakuba, 2015: The energy balance over land and oceans: an
948 assessment based on direct observations and CMIP5 climate models. *Clim Dyn*, **44**, 3393–3429,
949 doi:10.1007/s00382-014-2430-z.

950 Wilson, K., and Coauthors, 2002: Energy balance closure at FLUXNET sites. *Agricultural and*
951 *Forest Meteorology*, **113**, 223–243, doi:10.1016/S0168-1923(02)00109-0.

952 Xie, P., and P. Arkin, 1997: Global precipitation: A 17-year monthly analysis based on gauge ob-
953 servations, satellite estimates, and numerical model outputs. *Bulletin of the American Meteoro-*
954 *logical Society*, **78**, 2539–2558, doi:10.1175/1520-0477(1997)078<2539:GPAYMA>2.0.CO;2.

955 **LIST OF TABLES**

956 **Table 1.** The reanalyses 46

957 **Table 2.** The gridded reference data sets. 47

958 **Table 3.** Global annual land average energy budget from the NASA reanalyses (Wm^{-2}),
959 estimated over an area of 130.2 million km². 48

TABLE 1. The reanalyses

Data set	Variables used	Output coverage and resolution (variable data set citation, where available)
MERRA-2	LH,SH, LW_{net} , SW_{net} LW_d T_{max}^{2m} , T_{min}^{2m}	1980-ongoing, hourly, $5/8^\circ \times 0.5^\circ$ global land (Global Modeling and Assimilation Office 2015b) global surface (Global Modeling and Assimilation Office 2015a) global surface (Global Modeling and Assimilation Office 2015c)
MERRA-Land	LH, SH, LW_{net}	1980-2016, hourly, $2/3^\circ \times 0.5^\circ$ global land (Global Modeling and Assimilation Office 2008c)
MERRA	LH,SH, LW_{net} , SW_{net} LW_d T_{max}^{2m} , T_{min}^{2m}	1979-2015, hourly, $2/3^\circ \times 0.5^\circ$ global land (Global Modeling and Assimilation Office 2008b) global surface (-) global surface (Global Modeling and Assimilation Office 2008a)
ERA-Interim	LH, SH	1979 - ongoing, monthly mean, 79 km global surface

TABLE 2. The gridded reference data sets.

Data set	Variables used	Output coverage and resolution	Dependencies, error estimates where available
GLEAM v3.1a	LH	1980-2016, daily mean, 0.25° global land	Uses a precipitation data set that includes CPCU (used in MERRA-2, MERRA-Land) and ERA-Interim precipitation, uses T^{2m} and radiation from ERA-Interim. <i>c.f.</i> tower obs., average ubRMSE: 20 Wm^{-2} , average R_{anom} : 0.42. Full details: Section 2.c.1.
MTE	LH, SH	1982-2011 monthly mean, 0.5° global land, excluding non-vegetated regions	Trained on an earlier generation of the Fluxnet-2015 data set. Uses a CRU-based T^{2m} data set, and CPCU precipitation (neither strongly influences temporal behavior). <i>c.f.</i> withheld tower obs., average RMSE: 15 Wm^{-2} (LH & SH), average R_{anom} 0.57 (LH), 0.60 (SH). Full details: Section 2.c.2.
CRU v4.00	$T_{min}^{2m}, T_{max}^{2m}$	1901-2015 monthly means 0.5° global land (data not informed by station obs. have been removed)	Input station obs. will overlap with T^{2m} assimilated into ERA-Interim. Locally, will be more uncertain where input station obs. are sparse. Full details: Section 2.c.3.
CERES-EBAF, vn 4.0	SW_d, SW_u, LW_d, LW_u	Mar. 2000-Feb. 2016 monthly mean, 1° global surface	Uses atmospheric profile and T_{skin} from same system as used in the NASA re-analyses (results in strong dependence for LW_u, LW_d). <i>c.f.</i> ground obs. average RMSE: 12 Wm^{-2} (SW_d), 10 Wm^{-2} (LW_d). Full details: Section 2.c.4.

960 TABLE 3. Global annual land average energy budget from the NASA reanalyses (Wm^{-2}), estimated over an
 961 area of 130.2 million km^2 .

	SW_d	SW_u	LW_d	LW_u	R_{net}	LH	SH
MERRA-2	204.6	40.7	312.6	385.5	91.0	47.8	42.2
MERRA-Land	as for MERRA			384.1	95.1	42.5	52.1
MERRA	206.5	40.9	313.7	386.7	92.6	50.4	41.2

962 **LIST OF FIGURES**

963 **Fig. 1.** The global annual mean energy budget over land from the reanalyses (MERRA-2 (M-2);
964 MERRA-Land (M-L); MERRA (M)), the literature (NEWS (NEW), Trenberth et al. (2009)
965 (Tre), Wild et al. (2015) (Wil), Jiménez et al. (2011) (Jim), Mueller et al. (2011) (Mu1), and
966 Mueller et al. (2013) (Mu3)), and the gridded reference data sets (MTE, GLEAM (GLM),
967 and CERES (CER)), for a) LH, b) SH, c) SW_d , d) SW_u , e) LW_d , f) LW_u , and g) R_{net} . For
968 NEW, Tre, and Wil, the land mean has been approximated from published continental means
969 as described in Section 2.b. Error bars are included where provided, for NEW and Wil these
970 span the possible range described by multiple products, and for Jim and Mu1 these represent
971 one standard deviation across multiple products (see citations for full details). 51

972 **Fig. 2.** R_{anom}^2 between monthly anomalies of LH and rootzone soil moisture (SM) in MERRA-2 for
973 JJA. No value is plotted where the correlation is negative. 52

974 **Fig. 3.** JJA sensitivity of the monthly mean T_{max}^{2m} to precipitation in MERRA-2: R_{anom}^2 between
975 the monthly mean T_{max}^{2m} anomalies, and the two-monthly (current + previous months) pre-
976 cipitation anomalies, for (a) the model-generated precipitation (PRECTOT), and (b) the
977 observation-corrected precipitation (PRECTOTCORR), together with their difference (c)
978 $\Delta R_{anom}^2 = R_{anom}^2(\text{PRECTOTCORR}, T_{max}^{2m}) - R_{anom}^2(\text{PRECTOT}, T_{max}^{2m})$. Values are plotted only
979 where the correlation between T_{max}^{2m} and precipitation is negative. 53

980 **Fig. 4.** The mean JJA turbulent fluxes, with GLEAM LH (column 1), MTE LH (column 2), and
981 MTE SH (column 3) reference data in row 1, and the difference from the reference data for
982 MERRA-2, MERRA-Land, and MERRA, in rows 2-4. The statistics span 1980-2016 for
983 GLEAM, and 1982-2011 for MTE. 54

984 **Fig. 5.** Separation of mean JJA turbulent flux into evaporative fraction (EF) and incoming radiation
985 biases, with the MTE EF (column 1), MTE LH+SH (column 2), and CERES-EBAF
986 (column 3) reference data in row 1, and the difference from the reference data for MERRA-
987 2, MERRA-Land, and MERRA in rows 2-4. The statistics span 1982-2011 for MTE, and
988 2000-2015 for CERES-EBAF. 55

989 **Fig. 6.** The mean JJA radiation terms, from the CERES-EBAF reference data (row 1), and differ-
990 ence from the reference data for MERRA-2 (row 1), for (columns 1-3) SW_{net} , LW_u , and LW_d .
991 The statistics span 2000-2015. 56

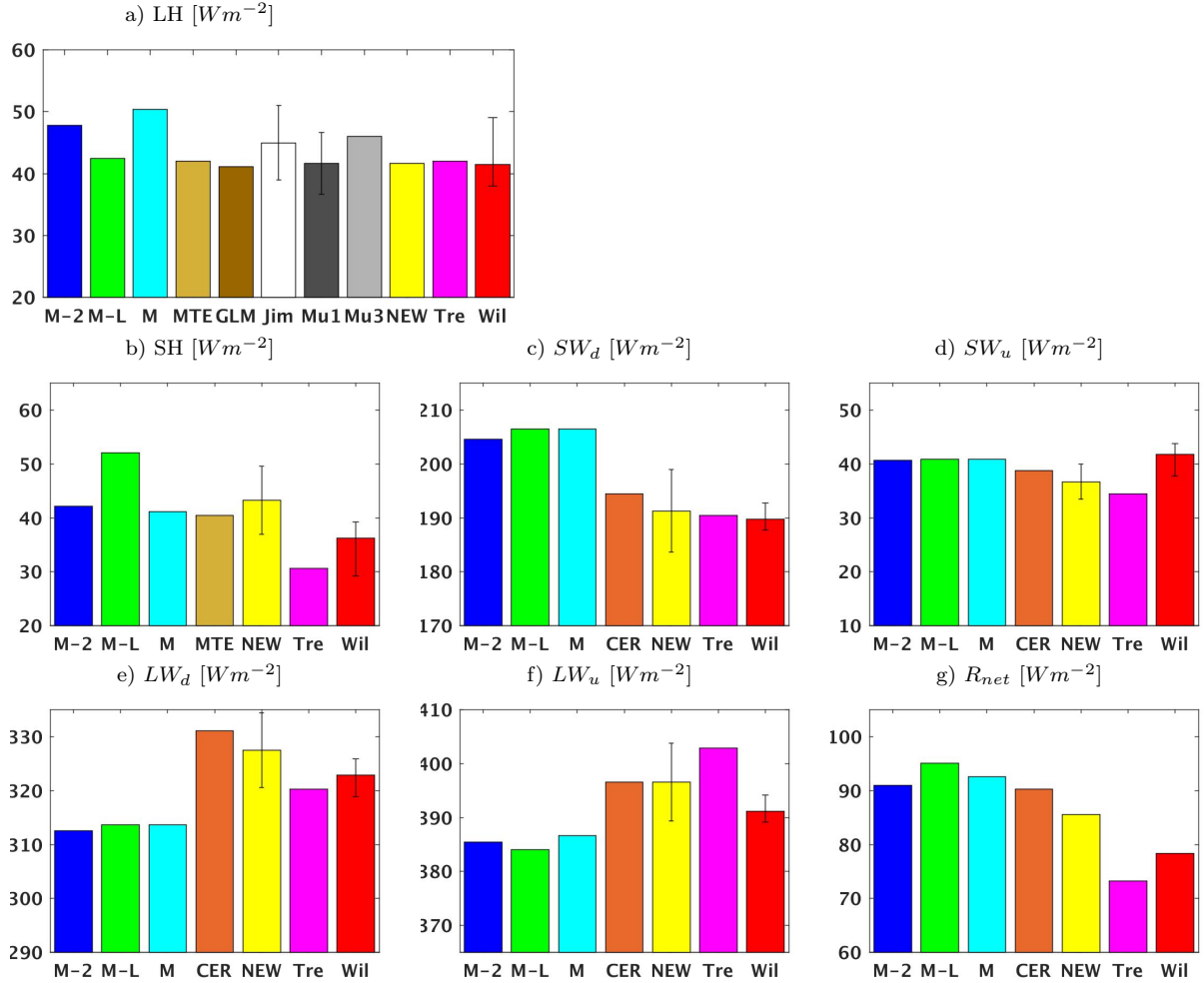
992 **Fig. 7.** The mean JJA T^{2m} , from CRU reference data (row 1), and the difference from the reference
993 data for MERRA and MERRA-2 (rows 2-3), for the T_{min}^{2m} (column 1), T_{max}^{2m} (column 2), and
994 the DTR (column 3). The statistics span 1980-2015, and white plotted over land indicates
995 insufficient CRU data. 57

996 **Fig. 8.** R_{anom} between GLEAM LH, MTE LH, and MTE SH (columns 1-3) for MERRA, MERRA-
997 Land, MERRA-2, and ERA-Interim (rows 1-4), for JJA. Statistics span 1980-2016 for
998 GLEAM and 1982-2011 for MTE. 58

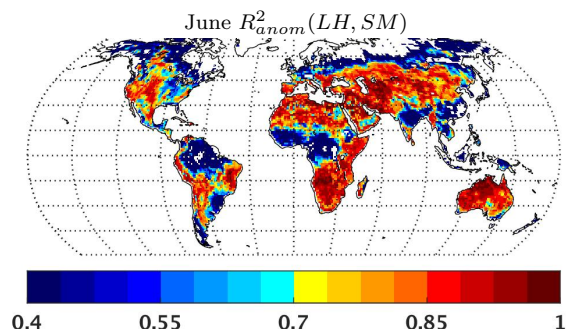
999 **Fig. 9.** Bar plot of the mean annual (a) LH and (b) SH, across the 20 Fluxnet site locations, from
1000 MERRA-2 (M-2), MERRA-Land (M-L), MERRA (M), Fluxnet (FIN), MTE, and GLEAM
1001 (GLM; LH only), calculated using each data set at its native resolution (and screened tem-
1002 porally for Fluxnet availability). For the global data sets, circles are plotted for the global
1003 land annual mean (taken from Figure 1). 59

1004 **Fig. 10.** Bar plot of the R_{anom} over JJA averaged across the 20 Fluxnet site locations, for (a) LH,
 1005 (b) SH, and (c) LH+SH, between each pair of the reanalyses (MERRA-2 (M-2), MERRA-
 1006 Land (M-L), MERRA (M), and ERA-I (E-I)) and the reference data (Fluxnet (FIN), MTE,
 1007 and GLEAM (GLM)). The R_{anom} vs. the Fluxnet reference data use the reanalysis output at
 1008 their reported spatial resolution (and screened temporally for Fluxnet availability), while the
 1009 R_{anom} vs. GLEAM and MTE use reanalyses and reference data regridded to 1° . For GLEAM
 1010 and MTE, circles are plotted for the global mean JJA R_{anom} (averaged over subplots of Figure
 1011 8). 60

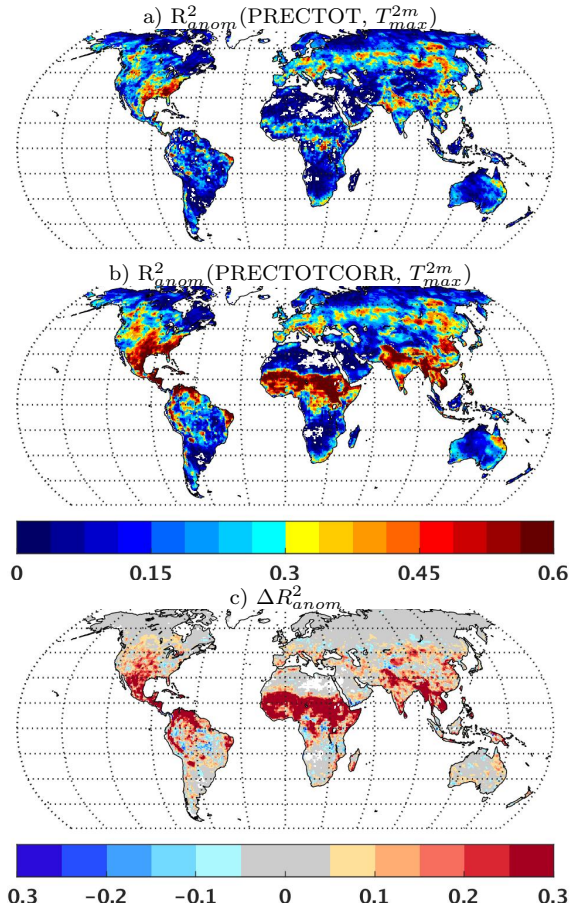
1012 **Fig. 11.** The (a) MERRA-2 R_{anom} vs. CRU monthly mean T_{max}^{2m} , and (b) the improvement in the T_{max}^{2m}
 1013 R_{anom} from MERRA to MERRA-2, both over JJA. Statistics span 1980-2015, and white
 1014 plotted over land indicates insufficient CRU data. 61



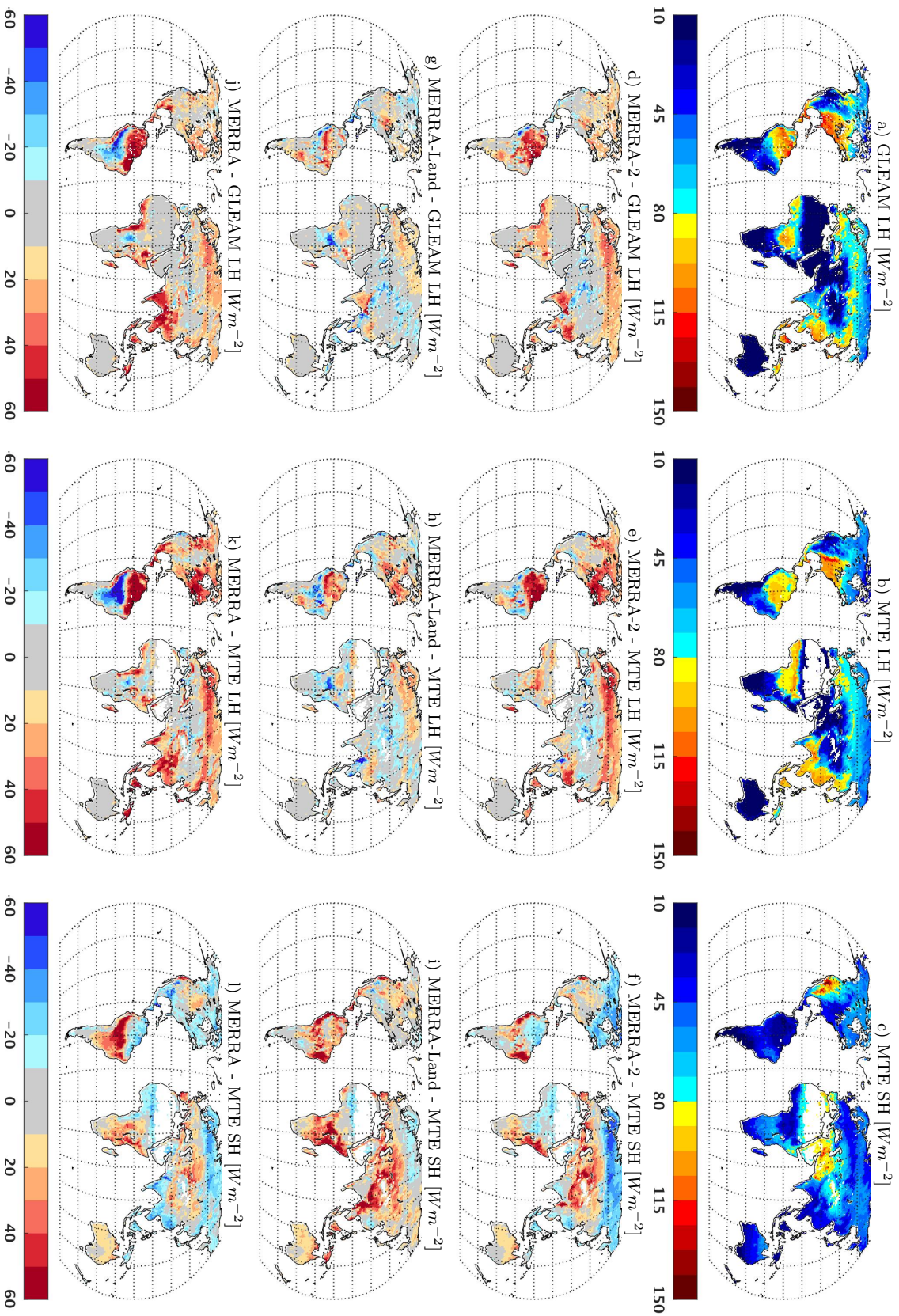
1015 FIG. 1. The global annual mean energy budget over land from the reanalyses (MERRA-2 (M-2); MERRA-
 1016 Land (M-L); MERRA (M)), the literature (NEWS (NEW), Trenberth et al. (2009) (Tre), Wild et al. (2015) (Wil),
 1017 Jiménez et al. (2011) (Jim), Mueller et al. (2011) (Mu1), and Mueller et al. (2013) (Mu3)), and the gridded
 1018 reference data sets (MTE, GLEAM (GLM), and CERES (CER)), for a) LH, b) SH, c) SW_d , d) SW_u , e) LW_d , f)
 1019 LW_u , and g) R_{net} . For NEW, Tre, and Wil, the land mean has been approximated from published continental
 1020 means as described in Section 2.b. Error bars are included where provided, for NEW and Wil these span the
 1021 possible range described by multiple products, and for Jim and Mu1 these represent one standard deviation
 1022 across multiple products (see citations for full details).



1023 FIG. 2. R_{anom}^2 between monthly anomalies of LH and rootzone soil moisture (SM) in MERRA-2 for JJA. No
1024 value is plotted where the correlation is negative.



1025 FIG. 3. JJA sensitivity of the monthly mean T_{max}^{2m} to precipitation in MERRA-2: R_{anom}^2 between the monthly
 1026 mean T_{max}^{2m} anomalies, and the two-monthly (current + previous months) precipitation anomalies, for (a) the
 1027 model-generated precipitation (PRECTOT), and (b) the observation-corrected precipitation (PRECTOTCORR),
 1028 together with their difference (c) $\Delta R_{anom}^2 = R_{anom}^2(\text{PRECTOTCORR}, T_{max}^{2m}) - R_{anom}^2(\text{PRECTOT}, T_{max}^{2m})$. Values are
 1029 plotted only where the correlation between T_{max}^{2m} and precipitation is negative.



1030 FIG. 4. The mean JJA turbulent fluxes, with GLEAM LH (column 1), MTE LH (column 2), and MTE SH (column 3) reference data in row 1, and the
 1031 difference from the reference data for MERRA-2, MERRA-Land, and MERRA, in rows 2-4. The statistics span 1980-2016 for GLEAM, and 1982-2011
 1032 for MTE.

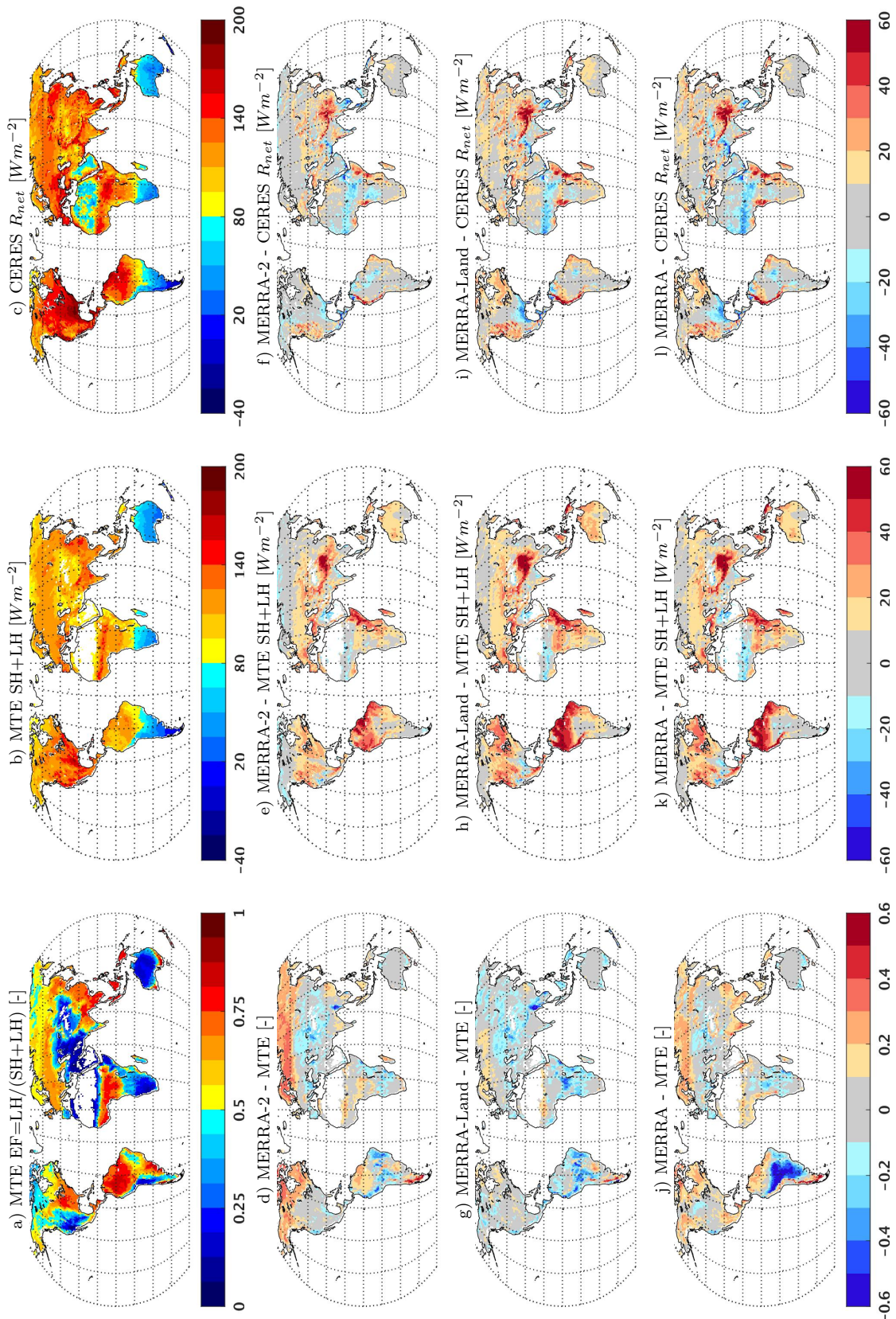
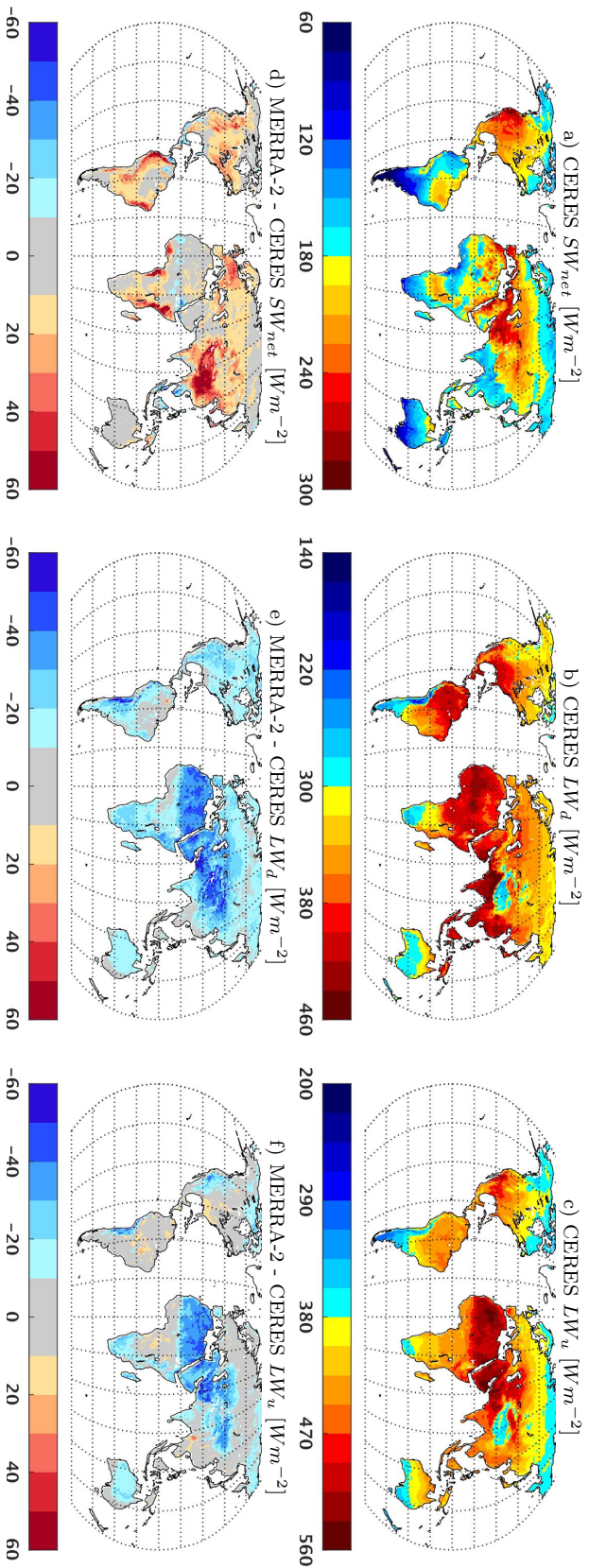


FIG. 5. Separation of mean JJA turbulent flux into evaporative fraction (EF) and incoming radiation biases, with the MTE EF (column 1), MTE LH+SH (column 2), and CERES-EBAF (column 3) reference data in row 1, and the difference from the reference data for MERRA-2, MERRA-Land, and MERRA in rows 2-4. The statistics span 1982-2011 for MTE, and 2000-2015 for CERES-EBAF.



1036 FIG. 6. The mean JJA radiation terms, from the CERES-EBAF reference data (row 1), and difference from the reference data for MERRA-2 (row 1),
 1037 for (columns 1-3) SW_{net} , LW_d , and LW_u . The statistics span 2000-2015.

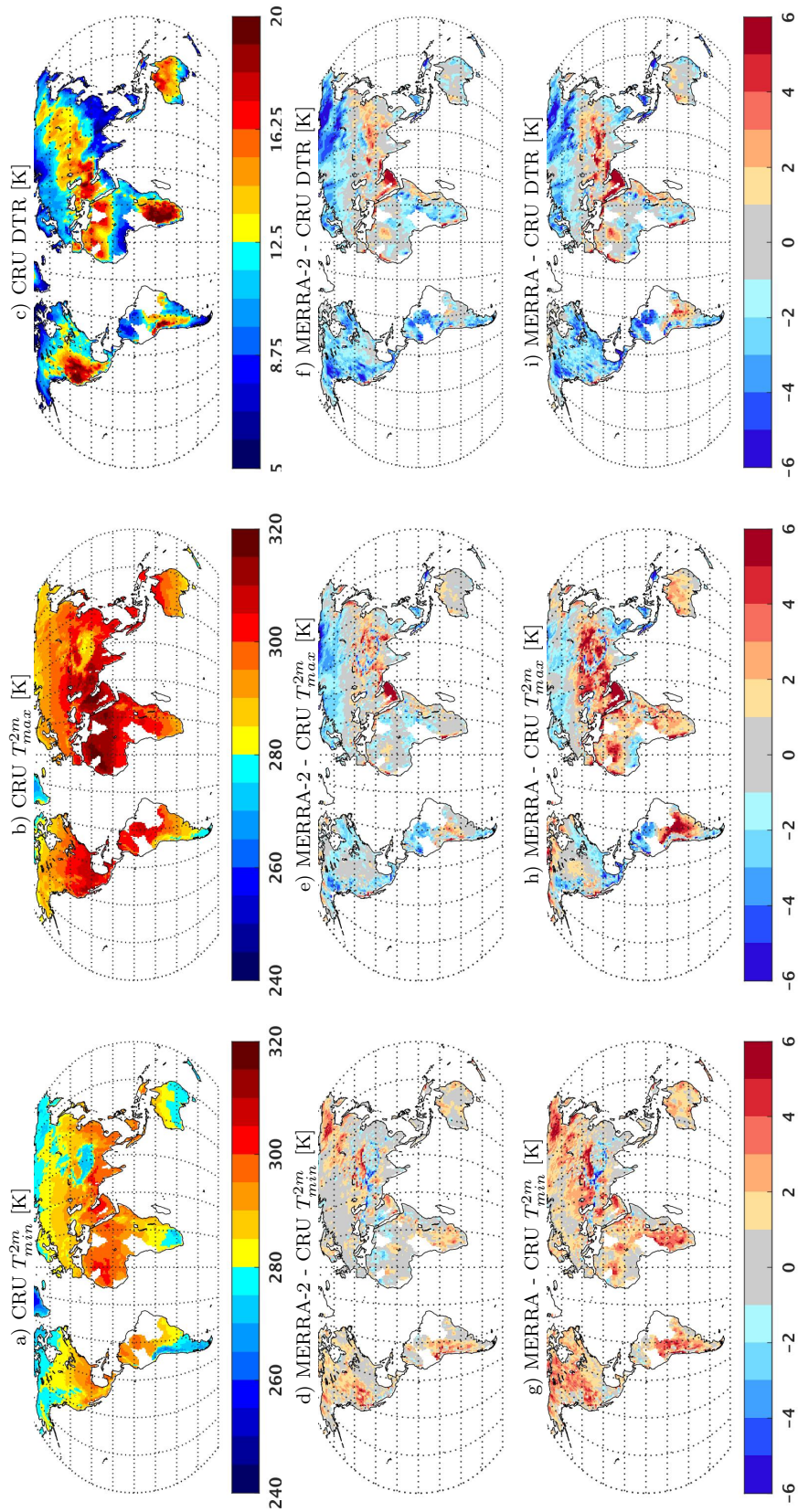
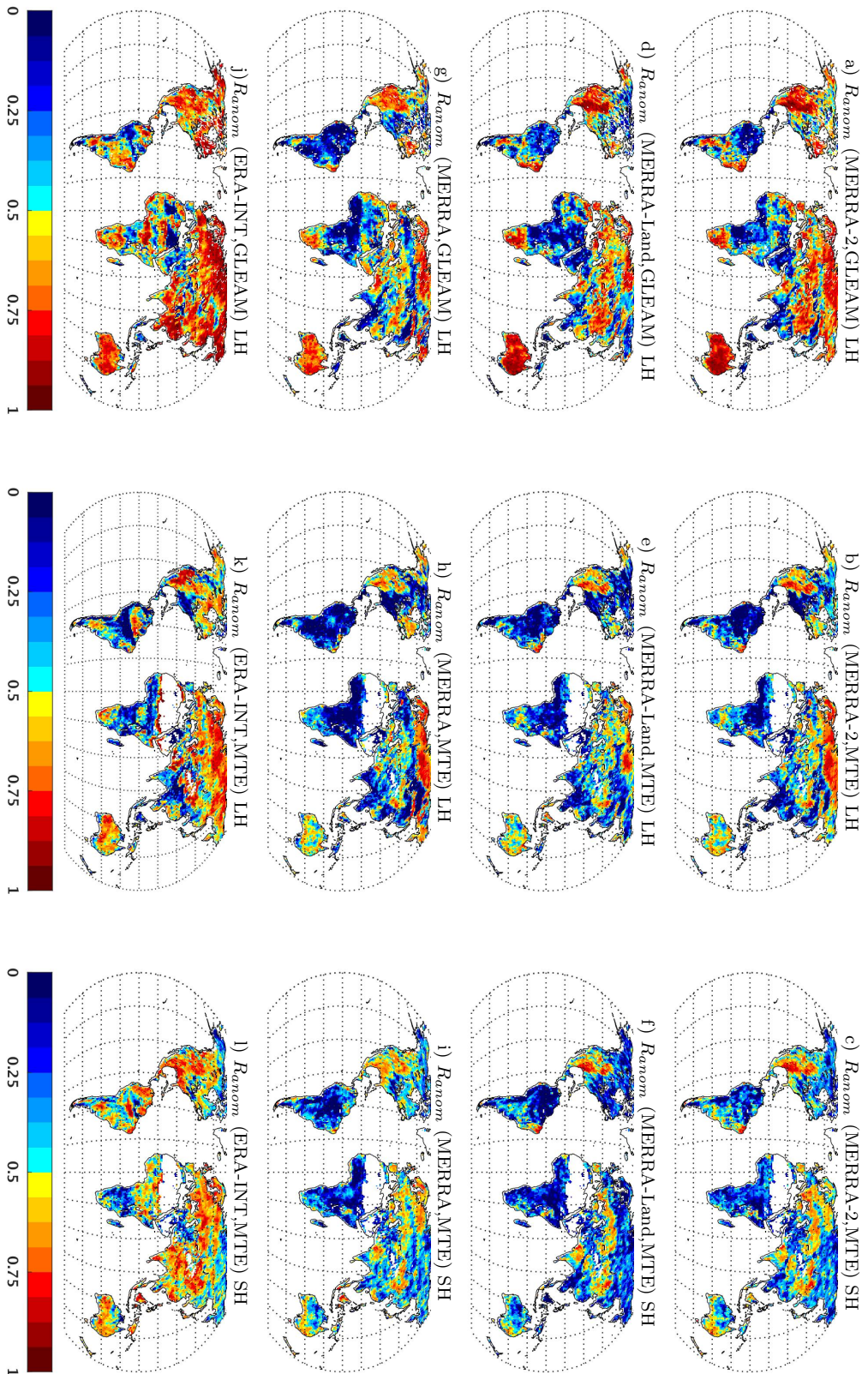
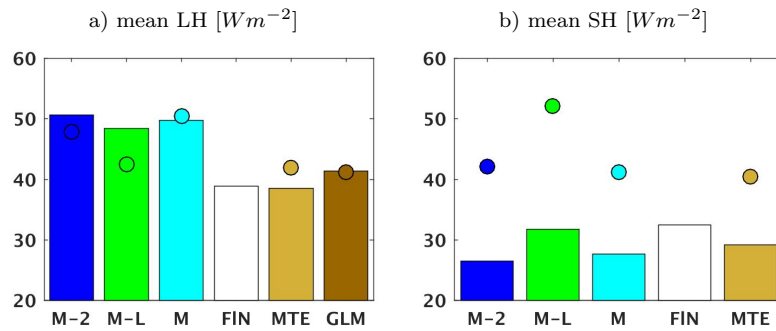


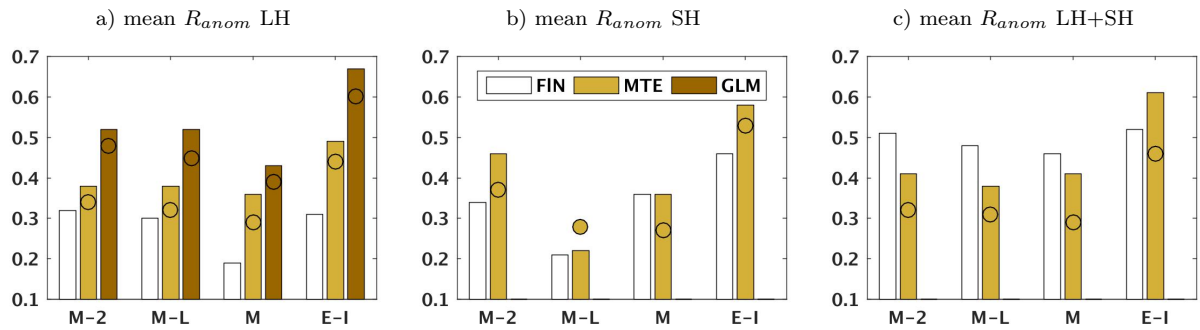
FIG. 7. The mean JA T_{min}^{2m} , from CRU reference data (row 1), and the difference from the reference data for MERRA and MERRA-2 (rows 2-3), for the T_{min}^{2m} (column 1), T_{max}^{2m} (column 2), and the DTR (column 3). The statistics span 1980-2015, and white plotted over land indicates insufficient CRU data.



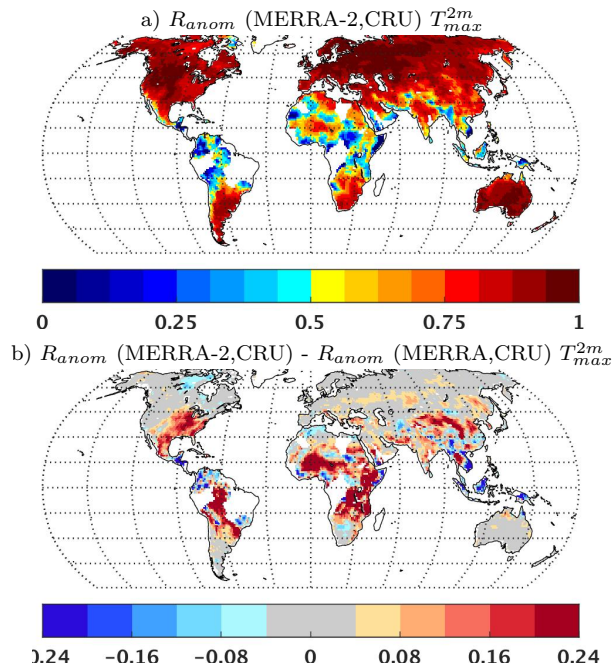
1041 **FIG. 8.** R_{anom} between GLEAM LH, MTE LH, and MTE SH (columns 1-3) for MERRA, MERRA-Land, MERRA-2, and ERA-Interim (rows 1-4),
 1042 for JJA. Statistics span 1980-2016 for GLEAM and 1982-2011 for MTE.



1043 FIG. 9. Bar plot of the mean annual (a) LH and (b) SH, across the 20 Fluxnet site locations, from MERRA-2
 1044 (M-2), MERRA-Land (M-L), MERRA (M), Fluxnet (FIN), MTE, and GLEAM (GLM; LH only), calculated
 1045 using each data set at its native resolution (and screened temporally for Fluxnet availability). For the global data
 1046 sets, circles are plotted for the global land annual mean (taken from Figure 1).



1047 FIG. 10. Bar plot of the R_{anom} over JJA averaged across the 20 Fluxnet site locations, for (a) LH, (b) SH,
 1048 and (c) LH+SH, between each pair of the reanalyses (MERRA-2 (M-2), MERRA-Land (M-L), MERRA (M),
 1049 and ERA-I (E-I)) and the reference data (Fluxnet (FIN), MTE, and GLEAM (GLM)). The R_{anom} vs. the Fluxnet
 1050 reference data use the reanalysis output at their reported spatial resolution (and screened temporally for Fluxnet
 1051 availability), while the R_{anom} vs. GLEAM and MTE use reanalyses and reference data regridded to 1° . For
 1052 GLEAM and MTE, circles are plotted for the global mean JJA R_{anom} (averaged over subplots of Figure 8).



1053 FIG. 11. The (a) MERRA-2 R_{anom} vs. CRU monthly mean T_{max}^{2m} , and (b) the improvement in the T_{max}^{2m} R_{anom}
 1054 from MERRA to MERRA-2, both over JJA. Statistics span 1980-2015, and white plotted over land indicates
 1055 insufficient CRU data.